

Learning-based Multi-View Stereo: A Survey

Fangjinhua Wang^{*†}, Qingtian Zhu^{*}, Di Chang^{*}, Quankai Gao, Junlin Han, Tong Zhang,
Richard Hartley, *Fellow, IEEE*, Marc Pollefeys, *Fellow, IEEE*

Abstract—3D reconstruction aims to recover the dense 3D structure of a scene. It plays an essential role in various applications such as Augmented/Virtual Reality (AR/VR), autonomous driving and robotics. Leveraging multiple views of a scene captured from different viewpoints, Multi-View Stereo (MVS) algorithms synthesize a comprehensive 3D representation, enabling precise reconstruction in complex environments. Due to its efficiency and effectiveness, MVS has become a pivotal method for image-based 3D reconstruction. Recently, with the success of deep learning, many learning-based MVS methods have been proposed, achieving impressive performance against traditional methods. We categorize these learning-based methods as: depth map-based, voxel-based, NeRF-based, 3D Gaussian Splatting-based, and large feed-forward methods. Among these, we focus significantly on depth map-based methods, which are the main family of MVS due to their conciseness, flexibility and scalability. In this survey, we provide a comprehensive review of the literature at the time of this writing. We investigate these learning-based methods, summarize their performances on popular benchmarks, and discuss promising future research directions in this area.

Index Terms—Multi-View Stereo, 3D Reconstruction, Deep Learning.

3D reconstruction describes the general task of recovering the 3D structure of a scene. It is widely applied in augmented/virtual reality (AR/VR), autonomous driving, and robotics [1]. The advancement of 3D acquisition techniques has led to the increased affordability and reliability of depth sensors, such as depth cameras and LiDARs. These sensors are extensively utilized for real-time tasks, enabling rough estimations of the surrounding environment, such as simultaneous localization and mapping (SLAM) [2]–[5] or dense reconstruction [6]–[8]. Nevertheless, depth maps captured by such sensors tend to be partial and sparse, resulting in incomplete 3D representations with limited geometric details. In addition, these sensors are active and usually consume a lot of power. In contrast, camera-based solutions, commonly found in edge devices like smartphones and AR/VR headsets, offer a more economically viable alternative for 3D reconstruction.

One fundamental technique in image-based 3D reconstruction is Multi-View Stereo (MVS). Given a set of calibrated

images, MVS aims to reconstruct the dense 3D geometry for an observed scene. Based on the scene representations, traditional MVS methods can be divided into three categories: volumetric, point cloud, and depth map. Volumetric methods [9]–[12] discretize the continuous 3D space into voxels and label each as inside or outside of the surface. They are limited to scenes of small scale because of the large memory consumption. Point cloud methods [13], [14] operate directly on 3D points and often employ propagation to gradually densify the reconstruction. As the propagation of point clouds is proceeded sequentially, these methods are difficult to be parallelized and thus take much time in processing [15]. In addition, the irregularity and large size of point cloud are also not very suitable for deep learning, especially in large-scale scenes. In contrast, methods relying on depth maps [16]–[20] use patch matching with photometric consistency to estimate the depth maps for individual images. Subsequently, these depth maps are fused into a dense representation, *e.g.*, point cloud or mesh, as a post-processing step. Such design decouples the reconstruction problem into per-view depth estimation and depth fusion, which explicitly improves the flexibility and scalability. Although MVS has been studied extensively for several decades, traditional MVS methods rely on hand-crafted matching metrics and thus encounter challenges in handling various conditions, *e.g.*, illumination changes, low-textured areas, and non-Lambertian surfaces [21]–[24].

To overcome these challenges, recent works [15], [25] have turned to learning-based methods, leveraging the emergence of Convolutional Neural Networks (CNNs) that have shown remarkable success in various 2D vision tasks. These learning-based MVS techniques have achieved remarkable success and explicitly outperform traditional methods [17], [18] on various benchmarks [21]–[23], [26], [27].

In this survey, we categorize existing learning-based MVS methods based on their characteristics as follows: depth map-based, voxel-based, NeRF-based, 3D Gaussian Splatting-based and large feed-forward methods. Voxel-based methods estimate the geometry with volumetric representation and implicit function, *e.g.*, Signed Distance Functions (SDF). They are limited to small-scale scenes due to the high memory consumption. NeRF and 3D Gaussian Splatting-based methods adapt NeRF [28] and 3D Gaussian Splatting [29], which are originally used for novel view synthesis, to extract surface from the implicit field or point cloud. They typically need to optimize the geometry for each new scene, which needs lots of run-time and memory consumption. Large feed-forward methods typically use large transformer models to directly learn the 3D representation from given images. They require massive computation because of the huge network, and are mainly

Fangjinhua Wang and Marc Pollefeys are with the Department of Computer Science, ETH Zurich, Switzerland.

Qingtian Zhu is with the Graduate School of Information Science and Technology, University of Tokyo, Japan.

Di Chang and Quankai Gao are with the Department of Computer Science, University of Southern California, USA.

Junlin Han is with the Department of Engineering Science, University of Oxford, UK.

Tong Zhang is with the School of Computer and Communication Sciences, EPFL, Switzerland.

Richard Hartley is with Australian National University, Australia.

Marc Pollefeys is additionally with Microsoft, Zurich.

*: Equal contribution. †: Project lead.

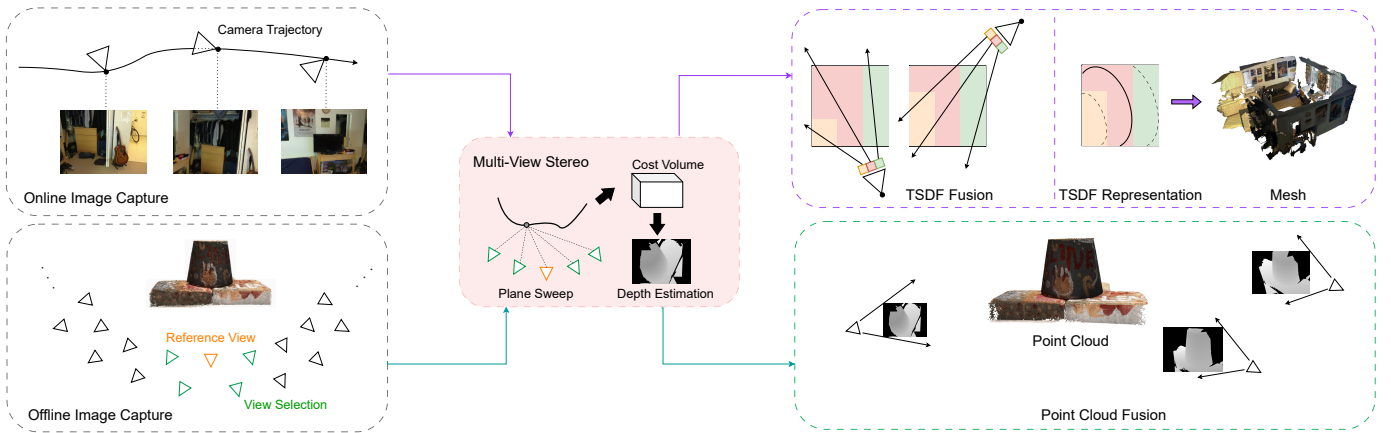


Fig. 1. An overall illustration of both online and offline depth map-based MVS pipelines. Online MVS usually deals with sequential data, *e.g.*, video, and employs TSDF volumes as an intermediate representation for mesh extraction. Given a full set of images, offline MVS holds the global information of the captured scene, and usually fuses estimated depth maps into a point cloud with filtering.

limited to object-level scenes [30]. Depth map-based methods utilize deep learning in depth estimation and then fuse depth maps with traditional fusion algorithm. Comparatively, depth map-based methods [15], [25] are the main family of learning-based methods since they inherit the advantages from those traditional methods [17]–[20] by decoupling 3D reconstruction into depth estimation and depth fusion. Therefore, we focus more on the depth map-based methods and discuss them in more details in this survey.

For clarity, we further categorize depth map-based methods into *online* and *offline* methods, shown in Fig. 1. Specifically, online MVS methods [25], [31] usually perform multi-view depth estimation with a video sequence of low-resolution images, *e.g.*, ScanNet [26]. They typically use small resolution inputs and a lightweight network structure to ensure quick inference considering speed and simplicity. The primary focus of online MVS is to provide instant reconstruction for applications where time efficiency is critical, *e.g.*, augmented reality and live video processing. In contrast, offline MVS methods [15], [32] prioritize better quality reconstruction at the cost of computation. These methods excel in multi-view depth estimation and point cloud fusion using high-resolution image sets, *e.g.*, DTU [21], Tanks and Temples [22] and ETH3D [23]. By operating on higher-resolution inputs and employing complex network designs, these approaches thoroughly analyze the multi-view information in the images. The emphasis on achieving high accuracy and capturing intricate details often comes at the cost of requiring considerable computational resources and time. As a result, offline MVS is frequently employed in applications demanding precise and photorealistic scene representations, including 3D modeling and archaeological reconstruction.

In summary, our survey covers the most recent literature on learning-based MVS methods until 2023, including four main families: depth map-based, voxel-based, NeRF-based, 3D Gaussian Splatting-based and large feed-forward methods. We provide a comprehensive review and insights on different aspects, including the pipelines and algorithmic intricacies. Moreover, we summarize the performance of the reviewed

methods on different benchmarks, and discuss the potential future directions for deep learning-based MVS methods.

I. PRELIMINARIES

Depth map-based MVS, including most traditional and learning-based methods, typically consists of several components: camera calibration, view selection, multi-view depth estimation and depth fusion. In this section, we introduce these components to provide readers a clear picture of the MVS problem. Note that camera calibration and view selection are components for other learning-based methods as well. Sec. I-A introduces camera calibration with Structure from Motion (SfM) or SLAM. Sec. I-B discusses how to select neighboring views to accurately reconstruct the geometry. Sec. I-C explains how to build cost volumes in learning-based MVS methods with plane sweep [33]. Sec. I-D introduces the typical depth fusion strategies after depth estimation. Sec. I-E lists common datasets and benchmarks for MVS and Sec. I-F summarizes the common evaluation metrics.

A. Camera Calibration

Camera calibration is a process of determining the intrinsic and extrinsic parameters of a camera to understand its geometry and characteristics accurately [55]. It serves as the foundational step in MVS, ensuring that the subsequent reconstruction process is built on accurate and consistent geometric information, ultimately leading to a more reliable and precise 3D representation of the scene. Typically, obtaining calibrated camera parameters is usually achieved by running off-the-shelf SfM algorithms [17], [56] or SLAM [57], which jointly optimize sparse triangulated 3D points and camera parameters. The camera parameters include the extrinsic matrix $\mathbf{T} = [\mathbf{R}|\mathbf{t}]$ and intrinsic matrix \mathbf{K} . Depth map-based MVS methods [15], [32], [40] require a bounded depth range $[d_{\min}, d_{\max}]$ to improve the estimation accuracy. For offline methods [15], [32], the depth range can be estimated by projecting the sparse point cloud from SfM to each viewpoint and compute the minimum and maximum z values [15]. In contrast, online methods [25],

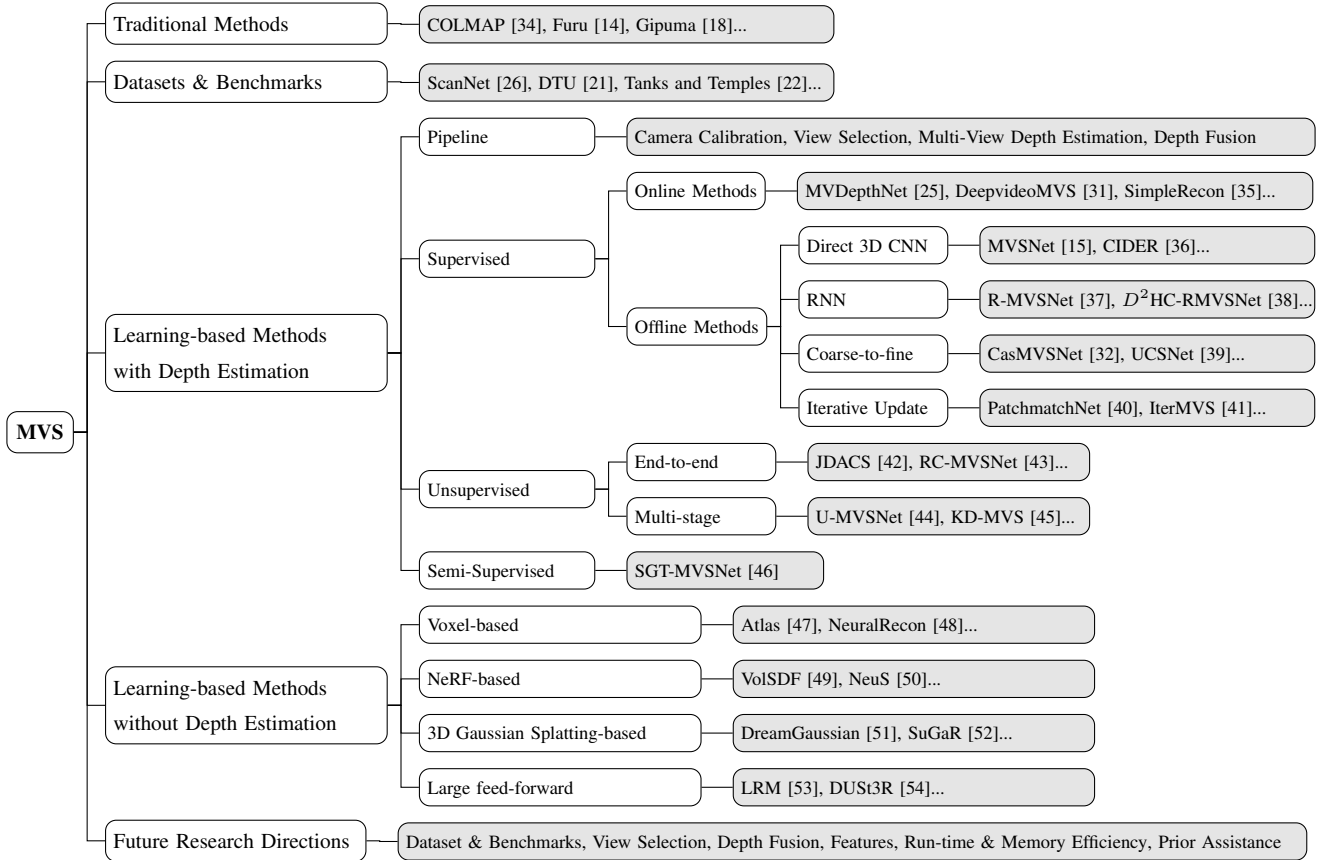


Fig. 2. Taxonomy of Multi-View Stereo.

[31] usually set constant depth ranges, *e.g.*, $[0.25m, 20.00m]$, since the scene scale is usually fixed as room.

B. View Selection

The selection of views is an important step for reconstruction. It is important to balance triangulation quality, matching accuracy, and view frustum overlap [31]. Currently, there are two main strategies for view selection.

First, for most online MVS depth estimation methods [25], [31], [58], a frame is selected as a keyframe when its pose has sufficient difference compared with the previous keyframe. Then each keyframe adopts several previous keyframes to estimate depth. GP-MVS [58] proposes a heuristic pose-distance measure as:

$$\text{disc}(\mathbf{T}_{ij}) = \sqrt{\|\mathbf{t}_{ij}\|^2 + \frac{2}{3}\text{tr}(\mathbf{I} - \mathbf{R}_{ij})}, \quad (1)$$

where $\mathbf{T}_{ij} = [\mathbf{R}_{ij} | \mathbf{t}_{ij}]$ is the relative transformation between view i and j . This strategy is used by many following methods [31], [35].

Second, for most offline MVS methods [15], [32], [37], view selection is done with the sparse point cloud obtained by Structure-from-Motion [34], [56]. For a reference view i , MVSNet [15] computes a score $s(i, j) = \sum_{\mathbf{P}} \eta(\theta_{ij}(\mathbf{P}))$ for the neighboring view j , where \mathbf{P} is a 3D point observed by both view i and j . $\theta_{ij}(\mathbf{P}) =$

$(180/\pi) \arccos((\mathbf{c}_i - \mathbf{P}) \cdot (\mathbf{c}_j - \mathbf{P}))$ represents the baseline angle for \mathbf{P} and $\mathbf{c}_i, \mathbf{c}_j$ are the camera centers. $\eta(\cdot)$ is a piece-wise Gaussian function [59] to favor a certain baseline angle θ_0 :

$$\eta(\theta) = \begin{cases} \exp\left(-\frac{(\theta - \theta_0)^2}{2\sigma_1^2}\right), & \theta \leq \theta_0 \\ \exp\left(-\frac{(\theta - \theta_0)^2}{2\sigma_2^2}\right), & \theta > \theta_0 \end{cases} \quad (2)$$

where $\theta_0, \sigma_0, \sigma_1$ are hyper-parameters. Then the view selection is done by choosing neighboring views with highest scores. Almost all the following offline MVS methods [32], [37], [40] use the same strategy.

C. Multi-view Depth Estimation with Plane Sweep

To form a structured data format that is more suitable for convolution operations, most learning-based MVS methods rely on the plane sweep algorithm [33] to calculate matching costs. The plane sweep algorithm discretizes the depth space with a set of fronto-parallel planes along the depth direction. This practice is deeply inspired by learning-based binocular stereo methods [60]–[62], which assess matching costs for a set of disparity hypotheses and subsequently estimate the disparity.

In a nutshell, the plane sweep algorithm in MVS entails iteratively sweeping planes through the object space, computing homographies between images, and selecting depth values

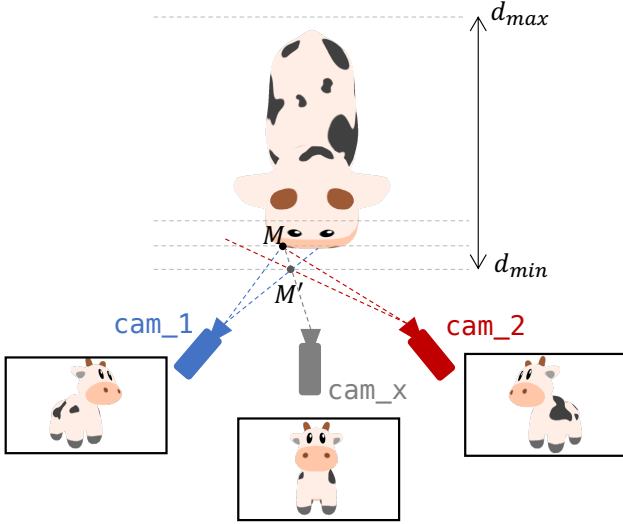


Fig. 3. Illustration of plane sweep algorithm [33]. To estimate the depth map for reference image (cam_x), neighboring source images (cam_1 , cam_2) are projected with homography to fronto-parallel planes of the reference view frustum.

based on consensus among different views, ultimately facilitating accurate 3D reconstruction. The plane sweep algorithm discretizes the depth space using a series of parallel planes along the depth direction. It operates by sweeping a conceptual plane through the object space and evaluating the spatial distribution of geometric surfaces. It is worth noting that, for learning-based MVS, plane sweep is conducted purely on GPU, and instead of warping hand-crafted features or edges, the dense pixels are efficiently warped.

We take a toy example of three cameras viewing the same object as illustrated in Fig. 3. Plane sweep is then performed on the frustum of cam_x (termed as the reference camera) by creating a series of fronto-parallel hypothesized planes within a given range (typically $[d_{\min}, d_{\max}]$), with each plane corresponding to a depth value *w.r.t.* cam_x . Let's then examine two 3D points, M and M' , as examples of occupied and unoccupied positions on hypothesized planes, respectively. For M , all of the three cameras capture the identical point lying on the geometry surface with photometric consistency. In contrast, the photometric consistency of the observations of M' are poor, indicating that M' is an invalid hypothesis. To evaluate the similarity of the observations towards M and M' , the images of cam_1 and cam_2 (termed as the source cameras) are warped to each plane by homography. These warped images are then compared against the scaled images of cam_x . Depth hypotheses with high similarity measures are considered reliable.

In practice, we divide the depth range, which is either manually set [25] or estimated by SfM [15], into discrete samples and assign hypotheses at these values. To map coordinates at depth hypothesis d , homography transformation [15] $\mathbf{p}_i(d) \sim \mathbf{H}_i(d) \cdot \mathbf{p}$, is applied, where $\mathbf{p}_i(d)$ is the corresponding pixel in the i -th source view for pixel \mathbf{p} of the reference view. The homography $\mathbf{H}_i(d)$ between the i -th source view and the

reference view 0 can be computed as:

$$\mathbf{H}_i(d) = \mathbf{K}_i \mathbf{R}_i \left(\mathbb{I} - \frac{(-\mathbf{R}_0^\top \mathbf{t}_0 + \mathbf{R}_i^\top \mathbf{t}_i) \mathbf{n}^\top \mathbf{R}_0}{d} \right) \mathbf{R}_0^\top \mathbf{K}_0^{-1}, \quad (3)$$

where \mathbf{K}_0 , \mathbf{K}_i denote camera intrinsics, $[\mathbf{R}_0 | \mathbf{t}_0]$, and $[\mathbf{R}_i | \mathbf{t}_i]$ denote camera extrinsics, \mathbf{n} denote the principle axis of the reference view. Equivalently, we can also project a reference pixel into source views with depth hypothesis [36], [40], [41]. We compute $\mathbf{p}_i(d)$ in the i -th source view for pixel \mathbf{p} in the reference and depth hypothesis d as follows:

$$\mathbf{p}_i(d) = \mathbf{K}_i \cdot (\mathbf{R}_i \mathbf{R}_0^\top \cdot (\mathbf{K}_0^{-1} \cdot \mathbf{p} \cdot d) - \mathbf{R}_i \mathbf{R}_0^\top \cdot \mathbf{t}_0 + \mathbf{t}_i). \quad (4)$$

The warped source feature maps are then obtained via differentiable interpolation.

Regarding selecting D depth hypotheses from the triangulated depth range $[d_{\min}, d_{\max}]$, there are two main schemes, namely the forward depth sampling and the inverse depth sampling. The naive forward sampling divides the depth range into $D-1$ depth intervals with identical lengths. Given a depth index k , we have

$$d_k = d_{\min} + \frac{k}{D-1} (d_{\max} - d_{\min}), k = 0, \dots, D-1, \quad (5)$$

where the depth hypotheses distribute uniformly between the two ends. While for the inverse sampling scheme [36], we sample uniformly in the multiplicative inverse of d , such that

$$\frac{1}{d_k} = \frac{1}{d_{\max}} + \frac{k}{D-1} \left(\frac{1}{d_{\min}} - \frac{1}{d_{\max}} \right), k = 0, \dots, D-1. \quad (6)$$

In this way, the distribution of sampled depth values becomes sparser with d approaching to d_{\max} . When reconstructing unbounded outdoor scenes, where the depth range is rather large, the inverse sampling will be a reasonable choice since it samples more densely at the foreground. In addition, as revealed in [63], the inverse sampling leads to a uniform sampling on the projected epipolar lines of source images.

So far, for each depth hypothesis made for cam_x , we have the warped source feature maps as well as the scaled reference feature map. The photometric similarity (or matching cost) is measured in a one-to-many manner between reference and warped source features for the following depth estimation, which will be discussed in Sec. II-B. By performing plane sweep, we obtain a cost volume with a regular spatial shape, making it easy for CNNs to process in parallel.

D. Depth Fusion

For depth map-based MVS, after estimating all the depth maps, we need to fuse them into a dense 3D representation, *e.g.*, point cloud or mesh. Online MVS methods [31], [35] usually adopt TSDF (Truncated Signed Distance Function) fusion [64], [65] to fuse the depth maps into a TSDF volume and then use Marching Cube [66] to extract the mesh. However, there usually exist outliers in the depth maps, which may reduce the reconstruction accuracy. To overcome this problem and improve the accuracy, offline MVS methods [15], [32], [40] typically filter the depth maps before fusing into a point cloud, which is motivated by Galliani *et al.* [18]. There are

TABLE I
AN OVERVIEW OF COMMONLY USED DATASETS AND BENCHMARKS FOR LEARNING-BASED MULTI-VIEW STEREO.

Dataset	Provided Ground Truth ¹				Synthetic	Online Benchmark	Evaluation Target
	Camera pose	Depth Map	Point Cloud	Mesh			
ScanNet [26]	✓	✓		✓			Depth Map / Mesh
7-Scenes [27]	✓	✓					Depth Map
DTU [21]	✓		✓				Point Cloud
Tanks and Temples [22]			✓			✓	Point Cloud
ETH3D [23]	✓		✓			✓	Point Cloud
BlendedMVS [24]	✓	✓			✓		Depth Map

¹ For datasets with online benchmark, the point cloud ground truth of test set is not released.

two main filtering steps: photometric consistency filtering and geometric consistency filtering [15]. For photometric consistency filtering, a per-pixel confidence, discussed in Sec. II-G, is estimated to measure the confidence of depth estimation, *i.e.*, probability that the ground truth depth is within a small range near the estimation. Then a threshold can be set to filter depth values with low confidence. For geometric consistency filtering, the consistency of depth estimations are measured among multiple views. For a pixel \mathbf{p} in the reference view 0, we project it to pixel \mathbf{p}' in its i -th neighboring view through its depth prediction $d_0(\mathbf{p})$. After looking up the depth for \mathbf{p}' , $d_i(\mathbf{p}')$, we re-project \mathbf{p}' back to the reference view at pixel \mathbf{p}'' and look up its depth $D_0(\mathbf{p}'')$. We consider pixel \mathbf{p} and its depth as consistent to the i -th neighboring view, if the distances, in image space and depth, between the original estimate and its re-projection satisfy:

$$\xi_d = \|\mathbf{p} - \mathbf{p}''\|_2 \leq \tau_1, \quad (7)$$

$$\xi_p = \frac{\|d_0(\mathbf{p}'') - d_0(\mathbf{p})\|}{d_0(\mathbf{p})} \leq \tau_2, \quad (8)$$

where τ_1 and τ_2 are thresholds. The pixels are considered to be reliable estimations if they are consistent in at least N neighboring views. Recently, instead of using predefined thresholds for τ_1 and τ_2 , dynamic consistency checking [38] is proposed to dynamically aggregate geometric matching error among all views and improve the robustness of reconstruction. Specifically, the dynamic multi-view geometric consistency $C_{\text{geo}}(\mathbf{p})$ is computed as:

$$C_{\text{geo}}(\mathbf{p}) = \sum_i \exp(-(\xi_p + \lambda \xi_d)), \quad (9)$$

where λ is a weight to balance the reprojection error in two metrics. Then the outliers with $C_{\text{geo}}(\mathbf{p})$ smaller than a threshold are filtered.

E. Datasets and Benchmarks

Tab. I is a brief summary of commonly used public MVS datasets and benchmarks for training and evaluation.

ScanNet: ScanNet [26] is a large RGB-D dataset that contains 1613 indoor scenes with ground-truth camera poses, depth maps, surface reconstruction and semantic segmentation labels. Online MVS methods [25], [31], [35] mainly use ScanNet for training and testing.

7-Scenes: 7-Scenes dataset [27] is a RGB-D dataset captured in indoor scenes with a handheld Kinect RGB-D camera. Since it is relatively small, 7-Scenes is usually used to test the generalization performance of the models trained on ScanNet [26] without finetuning.

DTU: DTU dataset [21] is an object-centric MVS dataset collected under well-controlled laboratory conditions with known accurate camera trajectory. It contains 128 scans with 49 or 64 views under 7 different lighting conditions. Since DTU dataset officially provides scanned ground truth point clouds instead of depth maps, it is required to generate mesh models with surface reconstruction, *e.g.*, screened Poisson surface reconstruction algorithm [67], and then render depth maps [15] for training.

Tanks and Temples: Tanks and Temples [22] is a large-scale benchmark captured in more complex real indoor and outdoor scenarios. It is divided into intermediate and advanced sets. Different scenes have different scales, surface reflection and exposure conditions. It is usually used to test the generalization performance. Note that Tanks and Temples does not provide ground truth camera parameters, which are usually estimated with Structure-from-Motion methods such as COLMAP [17] or OpenMVG [56].

ETH3D: ETH3D benchmark [23] contains 25 large-scale scenes, including indoor and outdoor, with high-resolution RGB images. The scenes typically contain many low-textured regions and non-Lambertian surfaces, *e.g.*, white walls and reflective floor. In addition, the images are usually sparse and have strong viewpoint variations and occlusions. Therefore, ETH3D is considered as a very challenging benchmark. Similar to Tanks and Temples, ETH3D is usually used to test the generalization performance.

BlendedMVS: BlendedMVS dataset [24] is a recently introduced large-scale synthetic dataset for MVS training that contains a variety of scenes, such as cities, sculptures and shoes. The dataset consists of over 17k high-resolution images rendered with reconstructed models and is split into 106 training scenes and 7 validation scenes. Since images are rendered through virtual cameras, the camera parameters are accurate enough for training.

F. Evaluation Metrics

As mentioned in Tab. I, based on the ground truth, *e.g.*, depth maps or point clouds, evaluation metrics can be catego-

rized into 2D metrics and 3D metrics.

1) *2D Metrics*: 2D depth-based metrics are commonly used by online MVS methods [25], [31] to evaluate the depth maps [68], [69]. We list the commonly used metrics as follows: mean absolute depth error (Abs), mean absolute relative depth error (Abs Rel), mean absolute inverse depth error (Abs Inv), and inlier ratio with threshold 1.25 ($\delta < 1.25$):

$$\begin{aligned} \text{Abs} &= \frac{1}{N} \sum_{\mathbf{p}} |d(\mathbf{p}) - \hat{d}(\mathbf{p})|, \\ \text{Abs Rel} &= \frac{1}{N} \sum_{\mathbf{p}} \frac{|d(\mathbf{p}) - \hat{d}(\mathbf{p})|}{d(\mathbf{p})}, \\ \text{Abs Inv} &= \frac{1}{N} \sum_{\mathbf{p}} \left| \frac{1}{d(\mathbf{p})} - \frac{1}{\hat{d}(\mathbf{p})} \right|, \\ \text{Inlier Ratio} &= \frac{1}{N} \sum_{\mathbf{p}} \mathbb{1} \left[\frac{d(\mathbf{p})}{1.25} < \hat{d}(\mathbf{p}) < 1.25d(\mathbf{p}) \right], \end{aligned} \quad (10)$$

where $d(\mathbf{p})$ denotes the ground truth depth, $\hat{d}(\mathbf{p})$ denotes the estimation, N denotes the number of pixels with valid depth measurements and $\mathbb{1}[\cdot]$ denotes the indicator function.

2) *3D Metrics*: 3D point cloud evaluation is widely used by offline MVS methods [15], [37]. Note that the reconstructed point clouds should be aligned to ground truth point clouds before evaluation, *e.g.*, by Iterative Closest Point (ICP), if their extrinsics are differently calibrated.

Precision/Accuracy: Precision/Accuracy measures the percentage of predicted points that can be matched to the ground truth point cloud. Considering a point \mathbf{P}_p in the predicted point cloud, it is considered to have a good match in the ground truth point cloud $\{\mathbf{P}_g\}$ if

$$\|\mathbf{P}_p - \arg \min_{\mathbf{P} \in \{\mathbf{P}_g\}} \|\mathbf{P} - \mathbf{P}_p\|_2\|_2 \leq \lambda, \quad (11)$$

where λ is a scene-dependent threshold assigned by datasets. Usually λ is set to a large value for large-scale scenes. Note that in some datasets, instead of being measured by percentage [22], [23], precision/accuracy is measured by mean or median absolute distance [21].

Recall/Completeness: Recall/Completeness measures the percentage of ground truth points that can be matched to the predicted point cloud. For a point \mathbf{P}_g in the ground truth point cloud, it is considered a good match in the predicted point cloud $\{\mathbf{P}_p\}$ if

$$\|\mathbf{P}_g - \arg \min_{\mathbf{P} \in \{\mathbf{P}_p\}} \|\mathbf{P} - \mathbf{P}_g\|_2\|_2 \leq \lambda. \quad (12)$$

Similar to precision/accuracy, recall/completeness is sometimes measured by the percentage of points [22], [23] and sometimes measured by mean or median absolute distance [21], whose definition is similar to Chamfer distance.

F-Score: The two aforementioned metrics measure the accuracy and completeness of predicted point clouds. However, each of these metrics alone cannot present the overall performance since different MVS methods adopt different assumptions. A stronger assumption usually leads to higher accuracy but lower completeness. If only precision/accuracy is reported, it would favor MVS algorithms that only include

estimated points of high certainty. On the other hand, if only recall/completeness is reported it would favor MVS algorithms that include everything, regardless of accuracy. Therefore, F-score, an integrated metric, is introduced [22], [23]. F-score is the harmonic mean of precision and recall. It is sensitive to extremely small values and tends to get more affected by smaller values, which means that F-score does not encourage imbalanced results. However, in most cases, F-score still suffers from unfairness due to the limitations of ground truth, *e.g.*, sparse and incomplete point clouds may penalize for filling in the areas that are not present in the ground truth [47].

II. SUPERVISED METHOD WITH DEPTH ESTIMATION

This section mainly introduces supervised learning-based MVS methods with depth estimation. A typical depth map-based MVS pipeline mainly consists of the feature extraction (Sec. II-A), cost volume construction (Sec. II-B), cost volume regularization (Sec. II-C) and depth estimation (Sec. II-E). The pipelines of MVDepthNet [25] and MVSNet [15] are illustrated in Fig. 4 and Fig. 5, which are the representative methods of online and offline MVS methods respectively.

A. Feature Extraction

Considering efficiency, most methods use simple CNN structures to extract deep features from images, *e.g.*, ResNet [70], U-Net [71] and FPN [72]. For online MVS methods, feature extraction networks are usually used in line with the real-time operation goal. DeepVideoMVS [31] combines MNasNet [73], which is lightweight and has low latency, with FPN. SimpleRecon [35] proposes utilizing the first two blocks from ResNet18 [70] and an EfficientNet-v2 [74] encoder, which maintains efficiency and yields a sizeable improvement in depth map accuracy. For offline MVS methods, MVSNet [15] uses a stacked eight-layer 2D CNN to extract deep features for all the images. Coarse-to-fine methods further extract multi-scale features for estimation on multiple scales with FPN [32], [39], [40] or multi-scale RGB images [75], [76]. Recently, many following works have been paying more attention to feature extraction to improve the representation power of deep features. [77]–[79] introduce deformable convolutions to adaptively learn receptive fields for areas with varying richness of texture. CDS-MVSNet [80] uses a dynamic scale network, CDSFNet, to extract the discriminative features by analyzing the normal curvature of the image surface. GeoMVSNet [76] proposes a geometry fusion network that fuses the image features with coarse depth maps. With FPN as the main feature extractor, WT-MVSNet [81] and MVSFormer [82], further introduces Vision Transformers [83]–[85] for image feature enhancement. ET-MVSNet [86] integrates the Epipolar Transformer into the feature extraction, which performs non-local feature aggregation on the epipolar lines.

B. Cost Volume Construction

For both online and offline MVS methods, the cost volume is constructed with the plane sweep algorithm as discussed in Sec. I-C.

1) *Online MVS*: To reduce computation and improve the efficiency for online applications, online MVS methods usually construct 3D cost volumes $\mathbf{C} \in \mathbb{R}^{H \times W \times D}$, which store a single value as matching cost for each pixel \mathbf{p} and depth sample d_i . MVDepthNet [25] and GP-MVS [58] compute the per-pixel intensity difference between the reference and each source view as matching cost. If there is more than one source view, the cost volumes are averaged. Instead of intensity difference, Neural RGB-D [87] computes deep feature difference. DeepVideoMVS [31] and MaGNet [88] calculate the cost from pixel-wise correlation between the reference feature and the warped source feature. In addition to the dot product between reference image features and warped source image features, SimpleRecon [35] further adds metadata, *e.g.*, ray direction and relative pose, into the 4D cost volume. Then an MLP is used to reduce the dimension of 4D cost volume to a 3D cost volume.

2) *Offline MVS*: Offline MVS methods mainly focus on reconstructing high-quality dense geometry with high-resolution images. To encode more matching information and improve the quality, offline methods [15], [32] usually construct 4D cost volumes $\mathbf{C} \in \mathbb{R}^{H \times W \times D \times C}$, where each pixel \mathbf{p} and depth sample d_i is associated with a matching cost of dimension C . Since there may exist an arbitrary number of source views and serious occlusion [23], robustly aggregating matching information from all the source views is an important step. MVSNet [15] proposes a variance-based cost metric as follows:

$$\mathbf{C} = \text{Var}(\mathbf{V}_0, \dots, \mathbf{V}_{N-1}) = \frac{\sum_{i=0}^{N-1} (\mathbf{V}_i - \bar{\mathbf{V}})^2}{N}, \quad (13)$$

where $\{\mathbf{V}_i\}_{i=0}^{N-1}$ are (warped) feature volumes, $\bar{\mathbf{V}}$ is the average feature volume. To further reduce dimension, CIDER [36] adopts group-wise correlation [89] to compute a lightweight cost volume between reference and each warped source view. Then $N - 1$ cost volumes are averaged for regularization. Without considering occlusions, these methods consider all source views equally with the averaging operation.

Nonetheless, it is essential to emphasize that *occlusions* are crucial to consider, as they pose common challenges in MVS, frequently leading to invalid matching and inaccurate estimations [34]. Incorporating visibility information to aggregate matching details from source views can substantially bolster robustness against occlusions, thereby enhancing the accuracy of the reconstruction process [34].

To estimate view weights for source views, PVA-MVSNet [90] applies gated convolution [91] to adaptively aggregate cost volumes. View aggregation tends to give occluded areas smaller weights and the reweighting map is yielded according to the volume itself. Vis-MVSNet [92] aggregates pair-wise cost volumes by weighted sum, where the weight is negatively related to the uncertainty of depth probability distribution. [40], [41], [63] utilize pixel-wise view weight networks to learn view weights from the pair-wise cost volumes without supervision.

C. Cost Volume Regularization

Usually, the raw cost volume constructed from image features may be noisy and should be incorporated with smoothness constraint for depth estimation [15]. Therefore, cost volume regularization is an important step to refine the raw cost volume and aggregate matching information from a large receptive field.

1) *Online MVS*: A 2D encoder-decoder architecture is commonly used to aggregate information. MVDepthNet [25] and GP-MVS [58] concatenate the reference image and cost volume and send them to an encoder-decoder architecture with skip connections. In addition, GP-MVS [58] uses Gaussian process to fuse information from previous views. Neural-RGBD [87] accumulates depth probability volumes over time with a Bayesian filtering framework to effectively reduce depth uncertainty and improve robustness and temporal stability. DeepVideoMVS [31] applies 2D U-Net [71] on the cost volume and adds skip connections between the image encoder and cost volume encoder at all resolutions. It further uses ConvLSTM [93] to propagate past information with a small overhead of computation time and memory consumption. Long *et al.* [94] use MatchNet to regularize the cost volume and ContextNet to learn 2D context information from the reference view. By concatenating the cost volume and context feature, a hybrid volume is fed into the Epipolar Spatio-Temporal transformer to aggregate temporal information. SimpleRecon [35] fuses multi-scale image features, extracted from the pretrained EfficientNetv2 [74], into the cost volume encoder to improve the performance.

2) *Offline MVS*: Among most learning-based offline MVS methods that use 4D cost volumes, there are three main categories to perform cost volume regularization: direct 3D CNN, coarse-to-fine and RNN. Fig. 6 illustrates these three main schemes.

Direct 3D CNN: Similar to stereo estimation [60]–[62], 3D CNN is widely used for cost volume regularization in MVS [15], [36], [95]–[97]. As the blueprint of learning-based offline MVS methods, MVSNet [15] adopts a 3D U-Net [71] to regularize the cost volume, which aggregates context information from a large receptive field with relatively low computation cost. It is found that the 3D regularization can capture better geometry structures, perform photometric matching in 3D space, and alleviate the influence of image distortion caused by perspective transformation and occlusions [95]. However, since 3D CNN is memory and runtime consuming, many offline methods [15], [36], [95], [96] use limited depth hypotheses and estimate depth maps at low resolution.

RNN: Instead of 3D CNN, R-MVSNet [37] sequentially regularizes 2D slices of the cost volume along the depth dimension with a convolutional GRU [98], which is able to gather spatial and uni-directional context information in the depth dimension. D^2 HC-RMVSNet [38] augments R-MVSNet [37] with a complex convolutional LSTM [93]. AA-RMVSNet [77] further introduce an intra-view feature aggregation module for feature extraction and an inter-view cost volume aggregation module to adaptively aggregate cost volumes of different views. With sequential process of 2D slices, these methods

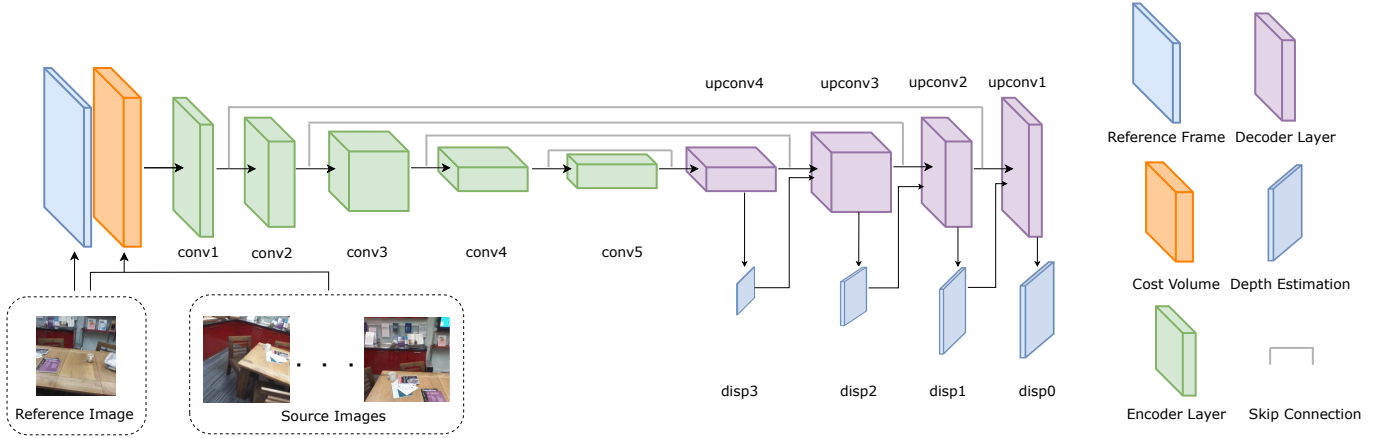


Fig. 4. Pipeline of MVDepthNet [25]. Multiple image frames are encoded in the cost volume. MVDepthNet takes the reference image and the cost volume as the input and outputs inverse depth maps of four different resolutions. Skip connections between the encoder and decoder of the same resolution are used for the per-pixel depth estimation.

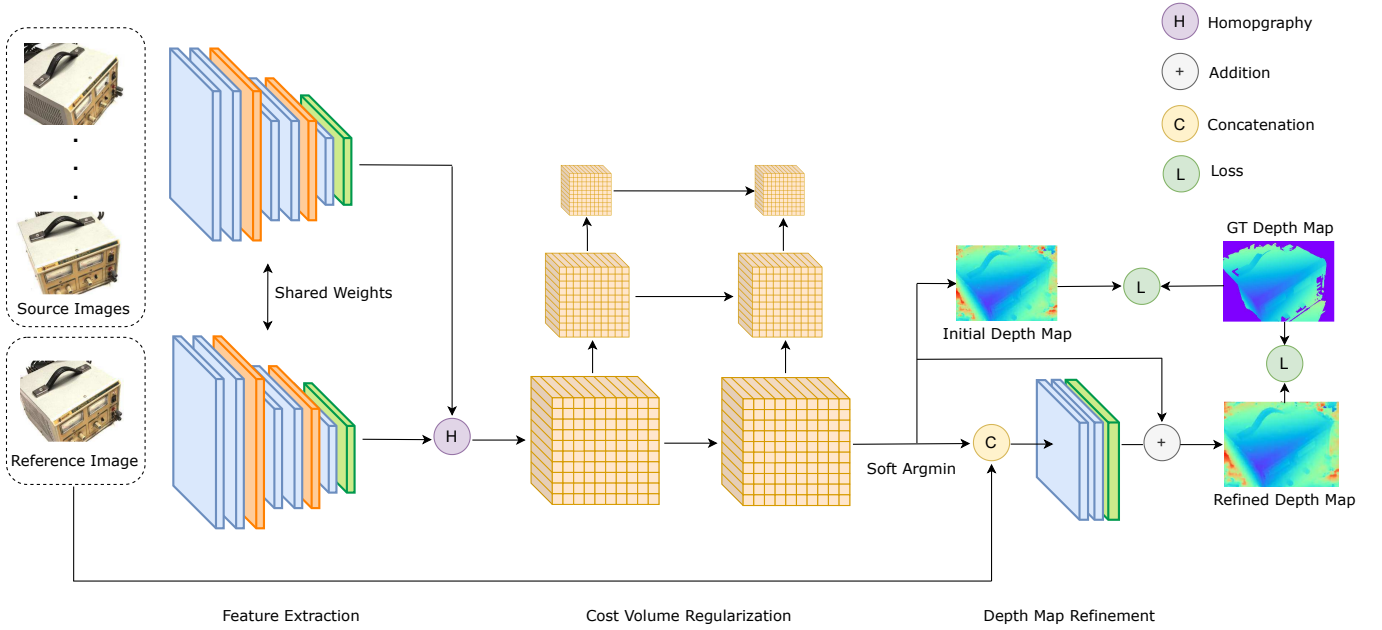


Fig. 5. Pipeline of MVSNet [15]. Reference and source images go through the feature extraction network, followed by the differentiable homography warping to construct the cost volume. A 3D U-Net is used to regularize the cost volume into a probability volume. The final depth map is estimated from the probability volume and refined with the reference image features.

improve the scalability for high-resolution reconstruction as well as large-scale scenes and reduce memory, however, at the cost of run-time.

Coarse-to-Fine: Predicting depth in a coarse-to-fine manner [32], [39], [40], [63], [75], [78], [99] is another solution of reducing both memory consumption and running-time. A coarse depth map is first predicted and then upsampled and refined during finer stages to construct fine details. CasMVSNet [32] constructs cascade cost volumes by warping features with reduced depth ranges around the previous coarse maps. Based on Eq. (3), the homography of differential warping at stage $k + 1$ is

$$\mathbf{H}_i^{(k+1)}(d^{(k)} + \Delta^{(k+1)}) = (d^{(k)} + \Delta^{(k+1)})\mathbf{K}_0\mathbf{T}_0\mathbf{T}_i^{-1}\mathbf{K}_i^{-1}, \quad (14)$$

where $d^{(k)}$ is the estimated depth value at stage k and

$\Delta^{(k+1)}$ is the residual depth to be determined in the current stage. Following MVSNet [15], 3D CNN is used on each stage to regularize the cost volume. UCS-Net [39] estimates uncertainty from the coarse prediction to adaptively adjust search ranges in finer stages. CVP-MVSNet [75] constructs the cost volume with a proposed optimal depth resolution of half pixel to narrow depth range in finer stages. EPP-MVSNet [100] introduces an epipolar-assembling module to assemble high-resolution information into cost volume and an entropy-based process to adjust depth range. TransMVSNet [79] uses a Feature Matching Transformer for robust long-range global context aggregation within and across images. WT-MVSNet [81] uses a window-based Epipolar Transformer for enhanced patch-to-patch matching, and a window-based Cost Transformer to better aggregate global information.

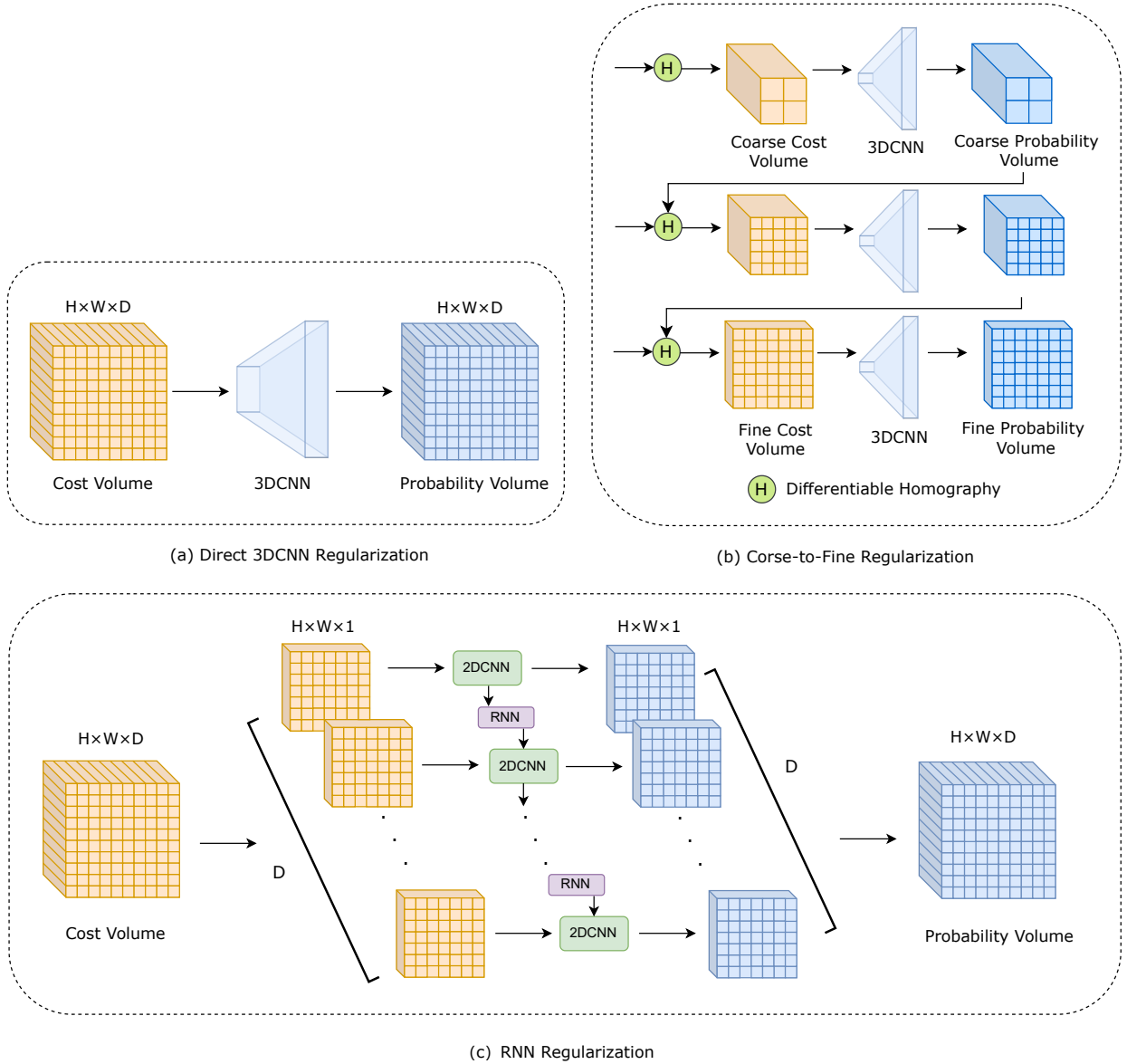


Fig. 6. Illustration of typical cost regularization schemes for offline MVS methods that use 4D cost volumes. (a) direct 3D CNN regularization [15], [36], [95], [96] applies a 3D CNN to aggregate contextual information; (b) coarse-to-fine regularization [32], [39], [63], [75] constructs multi-scale cost volumes based on coarse prediction and uses 3D CNN regularization on each scale; (c) RNN regularization [37], [38], [77] sequentially regularizes 2D slices of the cost volume to reduce memory consumption.

D. Iterative Update

Diverging from conventional approaches, certain methods [40], [41], [101], [102] adopt iterative updates to gradually refine depth maps. Iterative methods introduce a dynamic approach to depth map estimation, enabling iterative refinement of the reconstruction process. By iteratively updating the depth maps based on successive iterations, these methods can progressively improve the accuracy and consistency of the reconstructed 3D scene. This iterative refinement is particularly advantageous in scenarios where initial estimations may be coarse or inaccurate, as it allows for finer adjustments to be made to the depth maps over multiple iterations. Moreover, the ability to control the number of iterations provides users with the flexibility to prioritize either computational efficiency or reconstruction quality, depending on specific application

requirements.

Some methods [40], [103] combine iterative PatchMatch [104] with deep learning. PatchMatch algorithm is widely used in many traditional MVS methods [18], [19], [34], [105]. The PatchMatch algorithm mainly consists of: random initialization, propagation of hypotheses to neighbors, and evaluation for choosing best solutions. After initialization, the approach iterates between propagation and evaluation until convergence. Traditional methods usually design fixed patterns for propagation, *e.g.*, propagation of Gipuma [18] as shown in Fig. 7. Recently, PatchmatchNet [40] proposes learned adaptive propagation and cost aggregation modules, which enables PatchMatch to converge faster and deliver more accurate depth maps. Instead of propagating depth samples naively from a static set of neighbors as done traditionally [18],

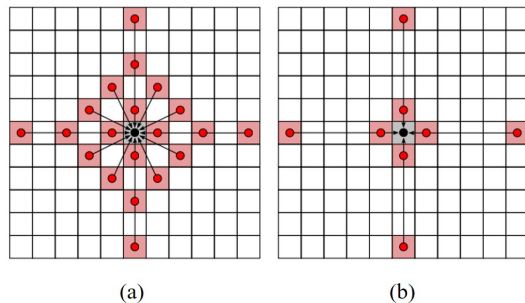


Fig. 7. Traditional chessboard propagation scheme of Galliani *et al.* [18]. Planes from a local neighborhood (red points) serve as candidates to update a given pixel (black). (a) Standard pattern with 20 neighbors. (b) Simplified pattern with 8 neighbors.

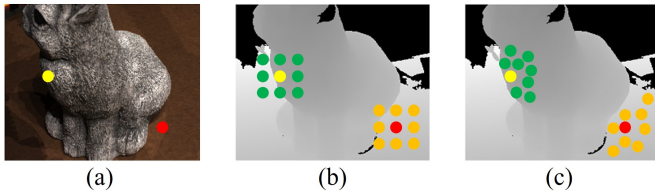


Fig. 8. Adaptive propagation scheme of Wang *et al.* [40]. Pixels located at the object boundary (yellow) and a textureless region (red) receive depth hypotheses from sampled neighbors (green and orange). (b) Fixed sampling locations of classic propagation. (c) Adaptive sampling locations with adaptive propagation. The grayscale image in (b) and (c) is the ground truth depth map.

PatchmatchNet adaptively gathers samples from pixels of the same surface with the guidance of image features, shown in Fig. 8. It iteratively updates the depth maps in a coarse-to-fine structure. Without 3D CNN, PatchmatchNet demonstrates a remarkably low computation time and memory than other coarse-to-fine methods [32], [39], [75]. Another PatchMatch-based method, PatchMatch-RL [103], jointly estimates depth, normal and visibility with a coarse-to-fine structure. Considering *argmax* based hard decisions/sampling of PatchMatch is non-differentiable, PatchMatch-RL adopts reinforcement learning in the training process.

Recently, RAFT [106] estimates optical flow by iteratively updating a motion field through a GRU and achieves state-of-the-art performance. The idea is further adopted in stereo [107], scene flow [108] and SfM [109]. In MVS, several methods [41], [101], [102] also adopted this approach to enhance efficiency and flexibility. IterMVS [41] proposes a lightweight GRU-based probability estimator that encodes the per-pixel probability distribution of depth in its hidden state. In each iteration, multi-scale matching information is injected to update the pixel-wise depth distribution. CER-MVS [101] and Effi-MVS [102] both embed the RAFT module in a coarse-to-fine structure. With the injection of matching information, the hidden state is updated and outputs a residual that is added to the previous depth estimation. DELS-MVS [110] proposes Epipolar Residual Network to search for the corresponding point in the source image directly along the corresponding epipolar line and follows an iterative manner to narrow down the search space. Based on IterMVS [41], RIAV-MVS [111]

iteratively refines index fields with a 3-level GRUs. MaGNet [88] iteratively updates the Gaussian distribution of depth for each pixel with the matching scores. IGEV-MVS [112] iteratively updates a disparity map regressed from geometry encoding cost volumes and pairs of group-wise correlation volumes.

E. Depth Estimation

1) *Online MVS*: Many methods [25], [31], [35], [58] apply encoder-decoder on the cost volume \mathbf{C} and reduce the feature channel to 1, *i.e.*, $\mathbf{C}' \in \mathbb{R}^{H \times W \times 1}$. Then the *sigmoid* activation σ is applied for normalization. Together with the predefined depth range $[d_{\min}, d_{\max}]$ (mostly manually set), the depth map can be computed. For example, DeepVideoMVS [31] estimates depth as:

$$\hat{d}(\mathbf{p}) = \left(\left(\frac{1}{d_{\min}} - \frac{1}{d_{\max}} \right) \cdot \sigma(\mathbf{C}'(\mathbf{p})) + \frac{1}{d_{\max}} \right)^{-1}, \quad (15)$$

where \mathbf{p} is the pixel coordinate. For other methods, Neural-RGBD [87] directly models the cost volume as probability volume \mathbf{P} and adopts *soft argmax* [60] to predict depth, Eq. (16). MaGNet [88] takes the mean of Gaussian distribution at last iteration as depth.

2) *Offline MVS*: For a cost volume $\mathbf{C} \in \mathbb{R}^{H \times W \times D \times C}$, a probability volume $\mathbf{P} \in \mathbb{R}^{H \times W \times D}$ is usually generated after cost volume regularization, which is then used for depth estimation. Currently, almost all the learning-based MVS methods use exclusively either regression (*soft argmax*) or classification (*argmax*) to predict depth.

Following GCNet [60], MVSNet [15] uses *soft argmax* to regress the depth map with sub-pixel precision. Specifically, the expectation value along the depth direction of probability volume \mathbf{P} is computed as the final prediction:

$$\hat{d}(\mathbf{p}) = \sum_{i=1}^D d_i \cdot \mathbf{P}(i, \mathbf{p}), \quad (16)$$

where \mathbf{p} is the pixel coordinate, d_i is i -th depth sample and $\mathbf{P}(i, \mathbf{p})$ is the predicted depth probability. For coarse-to-fine methods [32], [39], [75], *soft argmax* is applied on each stage to regress the depth maps. On the other hand, some methods [36], [40] compute the expectation value of *inverse* depth samples since this sampling is more suitable for complex and large-scale scenes [36]. The depth prediction is computed as:

$$\hat{d}(\mathbf{p}) = \left(\sum_{i=1}^D \frac{1}{d_i} \cdot \mathbf{P}(i, \mathbf{p}) \right)^{-1}. \quad (17)$$

In contrast, methods [37], [38], [77] that use RNN for cost volume regularization mainly adopt *argmax* operation. They choose the depth sample with the highest probability as the final prediction, which is similar to classification. Since the *argmax* operation adopted by winner-take-all cannot produce depth estimations with sub-pixel accuracy, the depth map may be refined in post-processing [37].

Comparatively, *soft argmax* operation corresponds to measuring the distance of the expectation to the ground truth depth. While the expectation can take any continuous value,

the measure cannot handle multiple modes in \mathbf{P} and strictly prefers unimodal distributions [41]. The *argmax* operation corresponds to measuring the Kullback-Leibler divergence between a one-hot encoding of the ground truth and \mathbf{P} , but cannot achieve sub-pixel precision [41]. Recently, Wang *et al.* [41] propose a simple yet effective hybrid strategy that combines regression and classification. Similar to [113], it is robust to multi-modal distributions but also achieves sub-pixel precision. First, similar to R-MVSNet [37], the index $\mathbf{X}(\mathbf{p})$ with the highest probability for pixel \mathbf{p} from probability \mathbf{P} is found. Then the expectation in the *local inverse* range is computed as the depth estimate $\hat{d}(\mathbf{p})$:

$$\hat{d}(\mathbf{p}) = \left(\frac{1}{\sum_{j=\mathbf{X}(\mathbf{p})-r}^{\mathbf{X}(\mathbf{p})+r} \mathbf{P}(j, \mathbf{p})} \sum_{j=\mathbf{X}(\mathbf{p})-r}^{\mathbf{X}(\mathbf{p})+r} \frac{1}{d_j} \cdot \mathbf{P}(j, \mathbf{p})} \right)^{-1}, \quad (18)$$

where d_j is the j -th depth sample. Concurrently, Peng *et al.* [114] propose a different strategy to unify regression and classification. They first use classification to get the optimal hypothesis and then regress the proximity for it.

DMVSNet [115] estimates two depth maps on multi-stages and composes the final depth map by alternating between selecting the maximum and minimum predicted depth values, which generates an oscillating depth map for improved geometry.

F. Depth Refinement

Given that the raw depth estimation from MVS may be noisy, refinement is usually used to improve the accuracy. R-MVSNet [37] enforces multi-view photo-consistency to alleviate the stair effect and achieve sub-pixel precision. PointMVSNet [95] and VA-Point-MVSNet [116] use PointFlow to refine the point cloud iteratively by estimating the residual between the depth of the current iteration and that of the ground truth. Fast-MVSNet [117] adopts an efficient Gauss-Newton layer to optimize the depth map by minimizing the feature residuals. PatchmatchNet [40] refines the final upsampled depth map with a depth residual network [118] and reference image feature. [41], [101], [102] use the mask upsampling module from RAFT [106] to upsample and refine the depth map to full resolution by computing the weighted sum of depth values in a window based on the mask. Based on a coarse depth map, RayMVSNet [119], [120] aggregates multi-view image features with an epipolar transformer and use a 1D implicit field to estimate the SDF of the sampled points and the location of the zero-crossing point. GeoMVSNet [76] filters the depth map by geometry enhancement in the frequency domain. EPNet [121] uses a hierarchical edge-preserving residual learning module to refine multi-scale depth estimation with image context features.

G. Confidence Estimation

As discussed in Sec. I-D, photometric confidence is important to filter out unreliable estimations during depth fusion for offline MVS methods. Following MVSNet [15], most offline MVS methods take the probability of the estimation [37], [38], [77] or the probability sum over several samples near

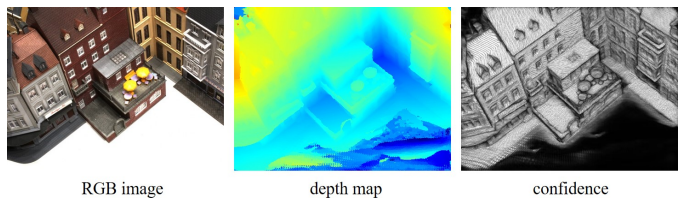


Fig. 9. Visualization of confidence on DTU [21]. The regions with low confidence typically correspond to occlusions and low texture.

the estimation [15], [32], [40] from the probability volume as confidence. Fig. 9 provides a set of RGB images, estimated depth maps, and the visualized confidence. In stereo matching, some methods learn confidence from disparity [122], RGB image [123], [124] or matching costs [125] and obtain confidence scores in $[0, 1]$ interval. Motivated by this, some traditional MVS methods [126], [127] based on classical PatchMatch [105] propose to estimate the confidence with deep learning and use this to refine the results from PatchMatch. Recently, IterMVS [41] estimates confidence from the pixel-wise depth probability distributions, which are encoded by the hidden state of a convolutional GRU. A 2D CNN followed by a *sigmoid* is applied to the hidden state to predict the confidence. DELS-MVS [110] feeds pixel-wise entropy of the partition probabilities, which is computed for each source image, into a confidence network to learn a confidence map. The confidence map is used to guide the fusion of multiple depth maps.

H. Loss Function

1) *Online MVS*: Many methods [25], [31], [58] compute the regression loss of estimated inverse depth maps for training:

$$L = \sum_{\mathbf{p}} \left\| \frac{1}{d(\mathbf{p})} - \frac{1}{\hat{d}(\mathbf{p})} \right\|_1, \quad (19)$$

where \mathbf{p} denotes the pixel coordinate, $d(\mathbf{p})$ denotes the ground truth depth, $\hat{d}(\mathbf{p})$ denotes the estimation and $\|\cdot\|_1$ denotes the L_1 loss. For other methods, Neural-RGBD [87] uses Negative-Log Likelihood (NLL) over the depth with its depth probability volume. Similarly, MaGNet [88] uses NLL loss since the per-pixel depth is modeled as Gaussian distribution. SimpleRecon [35] computes the regression loss with log-depth. To improve performance, SimpleRecon further uses gradient loss on depth, normal loss where normal is computed with depth and intrinsics, and multi-view regression loss.

2) *Offline MVS*: Based on the depth estimation strategy as discussed in Sec. II-E, loss functions can be mainly categorized into regression and classification. For methods [15], [36] that predict depth with *soft argmax* [60], (smooth) L_1 loss is usually adopted as the loss function, which is stated as:

$$L = \sum_{\mathbf{p}} \|d(\mathbf{p}) - \hat{d}(\mathbf{p})\|_1. \quad (20)$$

For coarse-to-fine methods [32], [39], [40], [75], the L_1 loss is computed on each stage for multi-stage supervision.

For methods [37], [38], [77] that predict depth with an *argmax* operation, cross entropy loss is commonly used for

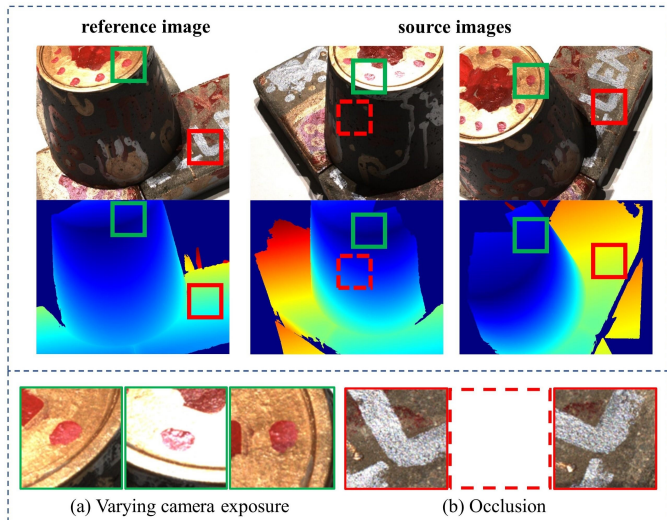


Fig. 10. Ambiguous supervision from photometric consistency assumption [43]. (a) Complicated lighting condition caused by varying camera exposures. (b) Invisibility of specific area caused by occlusion.

the loss function since the problem is multi-class classification. The cross entropy loss function is defined as:

$$L = \sum_{\mathbf{p}} \left(\sum_{i=1}^D -G(i, \mathbf{p}) \cdot \log[P(i, \mathbf{p})] \right), \quad (21)$$

where $G(i, \mathbf{p})$ is the ground truth one-hot vector of depth at pixel \mathbf{p} , and $P(i, \mathbf{p})$ is the predicted depth probability.

For methods that predict depth with a hybrid strategy of classification and regression, Wang *et al.* [41] adopt both L_1 loss and cross entropy loss to supervise the regression and classification respectively, while Peng *et al.* [114] use focal loss [128].

III. UNSUPERVISED & SEMI-SUPERVISED METHODS WITH DEPTH ESTIMATION

In this section, we introduce unsupervised learning-based MVS methods [42]–[44], [129], [130] and semi-supervised method [46]. Supervised MVS methods mentioned in Sec. II depend extensively on the availability of accurate ground truth depth maps obtained through depth-sensing equipment. This requirement not only complicates the data collection process, making it labor-intensive and costly but also restricts these methods to limited datasets and primarily indoor settings. To make MVS practical in more general real-world scenarios, it is vital to consider alternative unsupervised learning-based methods that can provide competitive accuracy compared to the supervised ones without any ground truth depth. Existing unsupervised methods are built upon the assumption of photometric consistency (Sec. III-A), which indicates that corresponding pixels from different views of the same 3D point share similar features. These approaches are categorized into end-to-end ones (Sec. III-B) and multi-stage ones (Sec. III-C). SGT-MVSNet [46] is the only semi-supervised method so far, and we introduce it in Sec. III-D. We also analyze the primary challenges in unsupervised MVS in Sec. III-B.

A. Photometric Consistency Assumption

In the realm of unsupervised depth map prediction, extant methods [44], [131]–[133] endeavor to establish photometric consistency between reference and source perspectives. This pivotal notion revolves around the augmentation of similarity between the reference image \mathbf{I}_0 and individual source images \mathbf{I}_i after their warping to align with the reference view.

In relation to the depth estimation denoted as \hat{d} for the initial image \mathbf{I}_0 , the process involves the projection of reference pixels into the subsequent image \mathbf{I}_i using the formulation presented in Eq. (4).

Subsequently, the distorted version of the source image denoted as $\hat{\mathbf{I}}_0^i$ is created by interpolating the RGB values of the source image at the displaced pixel positions through bilinear sampling. This interpolation is carried out at the locations where the pixels have been transformed due to the warping process. Additionally, alongside the warped image $\hat{\mathbf{I}}_0^i$, a binary mask M_i is commonly generated. This mask is employed to exclude pixels that have been projected beyond the boundaries of the image and are, thus, considered invalid.

The photometric consistency loss L_{PC} can be written as:

$$L_{PC} = \sum_{i=1}^{N-1} \frac{1}{\|M_i\|_1} \left(\left\| \left(\hat{\mathbf{I}}_0^i - \mathbf{I}_0 \right) \odot M_i \right\|_2 + \left\| \left(\nabla \hat{\mathbf{I}}_0^i - \nabla \mathbf{I}_0 \right) \odot M_i \right\|_2 \right), \quad (22)$$

where ∇ denotes the gradient at the pixel level, while \odot symbolizes element-wise Hadamard multiplication. In most cases [42]–[44], [131], [132], the incorporation of structural similarity loss and depth smoothness loss into the computation is commonplace. This practice aims to enhance the training process’s stability and speed up the convergence.

The computation of the structural similarity loss occurs between a synthesized image and the initial reference image, aiming to uphold contextual congruity. More precisely, the assessment of contextual similarity often involves the utilization of the Structural Similarity Index (SSIM) proposed by [134], a metric commonly employed for quantifying contextual consistency. This metric is defined as follows:

$$L_{SSIM} = \sum_{i=1}^{N-1} \left[1 - \text{SSIM} \left(\mathbf{I}_0, \hat{\mathbf{I}}_0^i \right) \right] \odot M_i, \quad (23)$$

$$\text{SSIM}(x, y) = \frac{(2\mu_x\mu_y + c_1)(2\sigma_{xy} + c_2)}{(\mu_x^2 + \mu_y^2 + c_1)(\sigma_x^2 + \sigma_y^2 + c_2)}, \quad (24)$$

where μ , σ^2 represent the mean and variance of the images, c_1, c_2 are constants to avoid numerical issues.

The incorporation of a smoothness loss term serves to promote the continuity of depth information within the context of image and depth disparity alignment. This continuity is evaluated based on the color intensity gradient present in the input reference image. The computation of the smoothness loss, L_{SM} , is defined as follows:

$$L_{SM} = \sum_{\mathbf{x}} \left| \nabla_u \tilde{d}(\mathbf{x}) \right| e^{-|\nabla_u \mathbf{I}_0(\mathbf{x})|} + \left| \nabla_v \tilde{d}(\mathbf{x}) \right| e^{-|\nabla_v \mathbf{I}_0(\mathbf{x})|}, \quad (25)$$

where ∇_u and ∇_v refer to the gradient along x and y axis, $\tilde{d} = d/\bar{d}$ is the mean-normalized inverse depth, M represents the set of valid pixels in the reference image.

B. End-to-end Unsupervised Methods

End-to-end methods [42], [43], [131], [135], [136] are those methods that are trained from scratch with the same input information as supervised methods (Sec. II), while not using ground truth depth for supervision. Instead, they usually adopt photometric consistency, structural similarity and smoothness constraint as parts of their loss terms. Unsup_MVS [131] proposes to inherit the supervision signal of view synthesis, as discussed in Sec. III-A, and dynamically select X “best” (lowest loss) values out of Y loss maps.

However, the bottleneck in unsupervised MVS is to find such accurate photometric correspondences. As illustrated in Fig. 10, in the real scenarios, non-Lambertian surfaces, varying camera exposures, and occlusions will make the assumption of photometric consistency invalid. Hence, such an invalid assumption will lead to “ambiguous supervision”.

To alleviate the ambiguous supervision, JDACS [42] introduces semantic consistency in addition to photometric consistency. It proposes to extract semantic features with a pre-trained network and create semantic classification map by applying non-negative matrix factorization. Then pixel-wise cross-view *segmentation* consistency is calculated. The difference here is that the semantic map is warped, instead of the image. In this way, the semantic classification maps are supervised by cross-entropy loss between the warped map S_i and reference map S_0 , both encoded as pixel-wise one-hot vector. However, the proposed semantic cross-view consistency loss is unstable to converge during training and such high-level semantic information excludes details and boundaries in MVS.

RC-MVSNet [43] digs into providing reliable and occlusion-aware supervision by introducing neural rendering. It takes the advantage of both strong representation ability of Neural Radiance Field [28] and strong generalization ability of cost volume. First, the unsupervised CasMVSNet [32] backbone in RC-MVSNet yields initial depth map supervised by photometric consistency. In addition, it generates depth priors for the Gaussian-Uniform mixture sampling in the rendering-consistency (RC) network. Then after volumetric rendering of the reference view, the depth map is supervised by an extra reference view synthesis loss and a depth rendering consistency loss. In this way, occlusion-aware neural rendering with mixture sampling is utilized to alleviate the invisibility phenomenon and ambiguous supervision from different lighting condition is solved by reference view synthesis.

ElasticMVS [135] introduces an architecture of part-aware patchmatch to address limitations in photometric loss-based geometry information, which tends to have missing data and artifacts in certain areas, particularly textureless regions. The proposed framework incorporates an elastic part representation to encode geometric details for guiding piecewise-smooth depth map prediction. The initial step involves the formal definition of part-aware representation. Building upon

this learned representation, enhancements are proposed for both depth hypotheses propagation and evaluation within the context of part-aware patchmatch. Finally, the network is optimized through the incorporation of a dense contrastive loss for self-supervised training, coupled with the integration of a spatial concentration loss [137] designed to promote the isotropic isolation of all pixel embeddings.

CL-MVSNet [136] proposes a framework that aims to enhance proximity among positive pairs by ensuring contrastive consistency between a regular branch and two contrastive branches. The regular branch is a CasMVSNet [32] structure that has been used in [42], [43], [135] as well, while contrastive branches incorporate an image-level branch and a scene-level branch. These branches enforce contrastive consistency guided by the confidence mask estimated from the regular branch. Additionally, the $L_{0.5}$ photometric consistency is proposed to enhance the accuracy of the reconstruction.

Note that these end-to-end methods are all trained from scratch without any pre-processing which saves training time and reduces the complexity of application in real scenarios.

C. Multi-stage Unsupervised Methods

Multi-stage methods require either pre-training of a specific module or pre-processing on the training data. These methods are built upon the idea of pseudo-label generation.

Self-supervised CVP-MVSNet [132] proposes to generate pseudo ground truth of depth by training the CVP-MVSNet [75] backbone with photometric consistency loss (Sec. III-A). The pseudo ground truth depth maps are refined with high-resolution images, filtered with cross-view depth consistency check and then fused in a point cloud [15]. Then the mesh is reconstructed with the screened Poisson surface reconstruction algorithm [67] to render complete pseudo depth maps for training in the next iteration. The whole pipeline consists of several iterations to improve the performance. However, [132] cannot provide a satisfying reconstruction of the 3D objects since it heavily relies on the photometric consistency assumption. Additionally, the self-training stage of the whole pipeline takes few days to complete.

U-MVSNet [44] introduces a flow-depth consistency loss by pre-training an optical-flow estimation network, PWC-Net [138], in an unsupervised manner. The dense 2D optical flow correspondences are used to generate pseudo labels for cross-view flow-depth consistency, which alleviates the ambiguous supervision in the foreground. Then the uncertainty-aware self-training consistency further reduces the invalid supervision in the background utilizing the generated pseudo labels and uncertainty map.

Recently, KD-MVS [45] achieves superior performance by leveraging a typical teacher-student scheme of knowledge distillation [139]–[141]. It trains a teacher MVS model, *e.g.*, MVSNet [15] or CasMVSNet [32], in a self-supervised manner, by enforcing both photometric and feature-metric consistency between the reconstructed and original images. Then the teacher model produces pseudo ground-truth labels of the training set by cross-view consistency check and probabilistic encoding. In addition to the reliable estimation by the teacher

model, the pseudo labels also contain probabilistic knowledge with estimation uncertainty. By training MVS networks [15], [32] with the pseudo labels, the knowledge of the teacher model is distilled to the student models.

D. Semi-supervised Methods

SGT-MVSNet [46] proposes to use only a few sparse ground truth 3D points to estimate the depth map of the reference view. 3D point consistency loss is used to minimize the difference between the 3D points back-projected from the corresponding pixels and the ground truth. To tackle the problem of inaccurate estimation on the edge and boundary, a coarse-to-fine reliable depth propagation module rectifies the erroneous predictions.

IV. LEARNING-BASED MVS WITHOUT DEPTH ESTIMATION

Though the learning-based methods that predict individual depth maps with plane-sweep are the main family of learning-based multi-view stereo, there are many methods of other families that achieve impressive 3D reconstruction quality in the recent years. In this section, We discuss four main families: voxel-based, NeRF-based, 3D Gaussian Splatting-based and large feed-forward methods.

A. Voxel-based Methods

These methods [47], [48], [142], [143] estimate the scene geometry with volumetric representation by leveraging implicit function, *e.g.*, SDF. Specifically, Atlas [47] and Neural-Recon [48] attempt to predict the TSDF volume from the 3D feature volume constructed by lifting 2D image features. As shown in Fig. 11, Atlas uses 3D CNN to regress the TSDF volume based on the feature volume accumulated from all images of the scene, which exhibits great completeness of reconstruction. The TSDF reconstruction is supervised using L_1 loss to the ground truth TSDF values. Since dense feature volume brings lots of computational overhead, NeuralRecon further improves the efficiency by incrementally reconstructing the scene in a fragment-wise and coarse-to-fine manner. The 3D features from different fragments are passed through the whole incremental reconstruction process with a RNN. TransformerFusion [142] fuses coarse and fine image features in a voxel grid with two transformers and then predicts an occupancy field to represent the scene geometry. VoRTX [143] uses a similar design to TransformerFusion and the scene geometry is obtained by passing three different-level features output from transformers through a 3D CNN.

B. NeRF-based Methods

In novel view synthesis, Neural Radiance Field (NeRF) [28] has kicked off a new emerging representation of 3D, which offers a differentiable volume-rendering scheme to supervise a 3D radiance-based representation with 2D image-level losses. The pipeline of NeRF is shown in Fig. 12. NeRF employs multi-layer perceptron (MLP) to map a position (x, y, z) and the normalized view direction (θ, ϕ) to the corresponding color

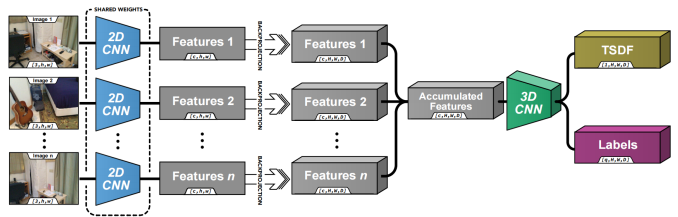


Fig. 11. Pipeline of Atlas [47]. 2D image features are back-projected into 3D volumes, which are aggregated and passed through a 3D CNN to directly regress a TSDF volume.

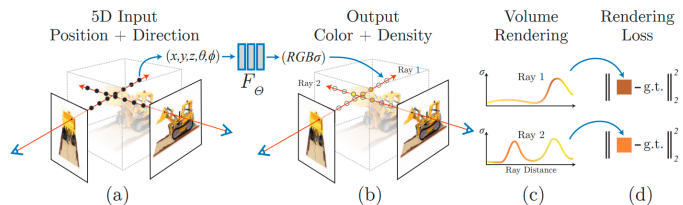


Fig. 12. Pipeline of NeRF [28]. Given a 3D position and 2D viewing direction (a), an MLP produces the color and volume density (b). Then volume rendering is used to composite these values into an image (c). The optimization is minimizing the rendering loss (d).

color \mathbf{c} and volume density σ . For a specific ray at a novel view-point, NeRF uses approximated numerical volume rendering to compute the accumulated color as:

$$\mathbf{C} = \sum_{i=1}^N T_i (1 - \exp(-\sigma_i \delta_i)) \mathbf{c}_i, \quad (26)$$

where i is the index of sample, $T_i = \exp(-\sum_{j=1}^{i-1} \sigma_j \delta_j)$ is the accumulated transmittance, and $\delta_i = t_{i+1} - t_i$ is the distance between adjacent samples. The model is trained by minimizing the loss between the predicted and ground truth color:

$$\mathcal{L}_{\text{color}} = \mathbb{E}[\|\mathbf{C} - \mathbf{C}_{gt}\|^2]. \quad (27)$$

Many subsequent endeavors [144]–[152] further improve NeRF in quality, fast training, memory efficiency and real-time rendering.

Though the initial purpose of NeRF is to perform novel view synthesis, VolSDF [49] and NeuS [50] integrate NeRF with SDF for surface reconstruction. The SDF, denoted as f , is transformed into the density σ for volume rendering. Specifically, for a point $\mathbf{p}(t)$, VolSDF computes the volume density $\sigma(\mathbf{p}(t))$ from the signed distance $f(\mathbf{p}(t))$ as:

$$\sigma(\mathbf{p}(t)) = \frac{1}{\beta} \Psi_{\beta}(-f(\mathbf{p}(t))), \quad (28)$$

where Ψ_{β} denotes the Cumulative Distribution Function (CDF) of a zero-mean Laplace distribution with learnable scale parameter $\beta > 0$. NeuS computes the density in a different way as:

$$\sigma(\mathbf{p}(t)) = \max\left(\frac{-f'(\mathbf{p}(t)) \Phi'_s(f(\mathbf{p}(t)))}{\Phi_s(f(\mathbf{p}(t)))}, 0\right), \quad (29)$$

where Φ_s is the sigmoid function with learnable scale parameter s . After training, the mesh can be extracted from the SDF field with Marching Cubes [66].

Note that without ground truth geometry supervision, *e.g.*, depth map or TSDF volume, these methods are trained in a self-supervised way as NeRF, Eq. (27). Since training with rendering loss only like NeRF has ambiguity in geometry [153], some following methods improve the reconstruction with explicit geometry supervision, *e.g.*, monocular depth/normal priors [154], [155] and sparse SfM point cloud [156]. Motivated by Instant-NGP [146] that accelerates training with hash grids, other methods [157]–[160] use hash grids to speed up training and improve surface details. In addition, to overcome the drawback that NeRF typically needs to be trained for each new scene, some recent methods [161]–[163] propose generalizable pipelines for implicit reconstruction even under sparse-view settings. Specifically, these methods project 3D points on the image planes and aggregate the corresponding image features as a feature volume like Atlas [47], which is used to estimate the surface location.

Recall that the depth map-based MVS methods predict depth with photometric consistency across multiple views. However, this assumption fails for glossy surfaces with reflections and thus they cannot reconstruct them accurately. In contrast, some NeRF methods can handle reflections well. Recently, Ref-NeRF [164] reparameterizes the appearance with separate diffuse and reflective components by using the reflected view direction, which improves the rendering of specular surfaces. Therefore, recent methods [160], [165]–[168] adopt this representation in reconstruction and can successfully reconstruct specular surfaces. Specifically, based on VolSDF / NeuS, these methods mainly replace the view direction with the reflected view direction following Ref-NeRF.

C. 3D Gaussian Splatting-based Methods

Unlike implicit representations with a coordinate-based MLP such as NeRF [169], 3D Gaussian Splatting [170] (3DGS) explicitly represents the scene with point primitives, each of which is parameterized as a scaled Gaussian with 3D covariance matrix Σ and mean μ :

$$G(\mathbf{x}) = e^{-\frac{1}{2}(\mathbf{x}-\mu)^T \Sigma^{-1}(\mathbf{x}-\mu)}, \quad (30)$$

where \mathbf{x} is an arbitrary position. Σ is formulated with a scaling matrix \mathbf{S} and rotation matrix \mathbf{R} as:

$$\Sigma = \mathbf{R} \mathbf{S} \mathbf{S}^T \mathbf{R}^T. \quad (31)$$

In addition, each Gaussian contains the color \mathbf{c} modeled by Spherical Harmonics and an opacity α . Different from NeRF that uses volume rendering, 3DGS efficiently renders the scene via tile-based rasterization. After projecting 3D Gaussian $G(\mathbf{x})$ into the 2D Gaussian $G'(x)$ on the image plane [170], a tile-based rasterizer efficiently sorts the 2D Gaussians and employs α -blending for rendering:

$$\mathbf{C}(x) = \sum_{i \in N} \mathbf{c}_i \sigma_i \prod_{j=1}^{i-1} (1 - \sigma_j), \quad \sigma_i = \alpha_i G'(x), \quad (32)$$

where x is the pixel location, N is the number of sorted 2D Gaussians. During training, 3DGS minimizes the rendering loss like NeRF, as in Eq. (27). 3DGS can be initialized with

SfM [17], [171] or MVS [34], which performs better than random initialization [170].

Motivated by the NeRF-based MVS methods, researchers try to adapt 3DGS for reconstruction. Though 3DGS achieves high-quality novel-view synthesis, it is challenging to recover high quality geometry since no explicit geometry constraint is used and 3D Gaussians do not correspond well to the actual surface because of the 3D covariance [52]. As one of the earliest methods, DreamGaussian [51] follows NeRF [28] to compute a dense density grid with the 3D Gaussians and then extracts mesh with Marching Cubes [66]. SuGaR [52] introduces a geometry regularization term encouraging the 3D Gaussians to be well-aligned over the scene surfaces so that the Gaussians can contribute to better scene geometry. To reconstruct the mesh, SuGaR samples 3D points on a level set of the density computed from 3D Gaussians and then runs Poisson Reconstruction [172] on these points. NeuSG [173] jointly trains Neuralangelo [158], a NeRF-based method, and 3DGS. During training, the normals from the SDF field of Neuralangelo regularize the rotation of 3D Gaussians, while the SDF field is regularized to ensure that the SDF values at 3D Gaussians' positions are close to zero. However, retrieving good geometry from Gaussian-based representations still needs to be explored.

D. Large Feed-forward Methods

In 3D reconstruction and 3D generation, a recent prominent trend is to directly learn the 3D representation from large-scale 3D datasets, such as Objaverse [30]. These methods typically adopt large-scale transformers [174] to generate a 3D representation based on various inputs, including single image [53], [175], [176], textual description [177], posed multi-view images [178], and un-posed multi-view images [54], [179]. LRM [53] uses a transformer-based feed-forward network to regress the 3D object from a single image. Specifically, LRM predicts features of a tri-plane representation [180], which is subsequently converted into an implicit field like NeRF [53]. Then the surface is extracted with Marching Cubes [66].

Recently, DUST3R [54] reconstructs the scene as a point cloud given a pair of un-calibrated and un-posed images. After extracting image token representations with Vision Transformer [181], two transformer decoders exchange information of the token representations via cross-attention and then regress the per-pixel 3D points in the coordinate frame of the first image. Many downstream tasks can be performed with the point clouds, *e.g.*, point matching, localization, intrinsic and relative pose estimation.

V. DISCUSSIONS

In this section, we summarize and discuss the performance of learning-based MVS methods, including supervised online methods with depth estimation (Sec. V-A), supervised offline methods with depth estimation (Sec. V-B), unsupervised methods with depth estimation (Sec. V-C) and methods without depth estimation (Sec. V-D). Moreover, we discuss potential directions for future research (Sec. V-E).

TABLE II
QUANTITATIVE RESULTS OF SUPERVISED ONLINE MVS METHODS ON SCANNET [26] AND 7-SCENES [27].

Methods	ScanNet [26]				7-Scenes [27]			
	abs ↓	abs-rel ↓	abs-inv ↓	$\eta < 1.25$ ↑	abs ↓	abs-rel ↓	abs-inv ↓	$\eta < 1.25$ ↑
MVDepthNet [25]	0.167	0.087	0.054	0.925	0.201	0.117	0.071	0.877
DPSNet [97]	0.219	0.119	0.071	0.868	0.249	0.149	0.085	0.826
Neural-RGBD [87]	0.236	0.122	0.075	0.850	0.214	0.131	0.076	0.865
GP-MVS [58]	0.149	0.076	0.049	0.940	0.174	0.100	0.064	0.903
Long <i>et al.</i> [94]	0.151	0.081	-	0.931	0.253	0.147	-	0.804
DeepVideoMVS [31]	0.119	0.060	0.038	0.965	0.145	0.038	0.054	0.938
MaGNet [88]	0.147	0.081	-	0.930	0.213	0.126	-	0.855
RIAV-MVS [111]	0.139	0.075	-	0.938	0.178	0.100	-	0.897
SimpleRecon [35]	0.089	0.043	-	0.981	0.105	0.058	-	0.974

TABLE III
QUANTITATIVE RESULTS OF POINT CLOUD EVALUATION ON MVS BENCHMARKS [21]–[23] FOR UNSUPERVISED DEPTH MAP-BASED MVS METHODS. “FINETUNED WITH BLENDEDMVS” DENOTES WHETHER THE METHODS ARE FINETUNED ON BLENDEDMVS [24] BEFORE EVALUATING ON TANKS AND TEMPLES [22].

Methods		DTU [21]			Finetuned with BlendedMVS [24]	Tanks and Temples [22]	
		Acc. ↓	Comp. ↓	Overall ↓		Intermediate F_1 ↑	Advanced F_1 ↑
End-to-end	Unsup_MVSNet [131]	0.881	1.073	0.977	✗	-	-
	MVS ² [129]	0.760	0.515	0.637	✗	37.21	-
	M ³ VSNet [130]	0.636	0.531	0.583	✗	37.67	-
	JDACS-MS [42]	0.398	0.318	0.358	✗	45.48	-
	RC-MVSNet [43]	0.396	0.295	0.345	✗	55.08	30.82
	ElasticMVS [135]	0.374	0.325	0.349	✗	57.88	37.81
	CL-MVSNet [136]	0.375	0.283	0.329	✗	59.39	37.03
Multi-stage	Self-supervised CVP-MVSNet [132]	0.308	0.418	0.363	✗	43.48	-
	U-MVSNet [44]	0.354	0.354	0.354	✗	57.15	30.97
	KD-MVS [45]	0.359	0.295	0.327	✓	64.14	37.96

A. Supervised Online MVS with Depth Estimation

Typically, online MVS methods are trained on ScanNet [26] and then evaluated on ScanNet [26] and 7-Scenes [27]. We summarize the quantitative results of online MVS methods in Tab. II. By incorporating temporal information in depth estimation, [31], [58], [94] achieve better performance than MVDepthNet [25]. However, this usually increase the network complexity. Instead of temporal fusion, SimpleRecon [35] injects cheaply available metadata into the cost volume and achieves state-of-the-art performance on both ScanNet and 7-Scenes.

B. Supervised Offline MVS with Depth Estimation

Offline MVS methods are usually trained on DTU [21] and then evaluated on DTU [21], Tanks and Temples [22] and ETH3D [23]. Recently, many methods further finetune the DTU-pretrained model on BlendedMVS [24] before evaluating on Tanks and Temples and ETH3D since it contains large-scale scenes.

1) *Benchmark Performance*: Tab. IV summarizes quantitative results of offline MVS methods. Compared with those methods that use direct 3D CNN for regularization,

the methods that use RNN and coarse-to-fine regularization perform much better. Since RNN based methods have bad time efficiency, we can find that coarse-to-fine methods become main stream of the community because of their impressive performance and high efficiency in both memory and run-time. In addition, iterative methods based on traditional PatchMatch [40], [103] or RAFT [41], [101], [102] also become popular since they achieve comparable performance as state-of-the-art methods with more lightweight structure. For benchmarks, most learning-based methods perform explicitly better than traditional methods on DTU and Tanks and Temples. However, on ETH3D, traditional methods [127], [189] perform better than all existing learning-based methods. We conjecture that the strong viewpoint variations and large textureless regions in human-made environments still make learning-based methods struggle. Therefore, it is valuable to pay more attention to ETH3D to evaluate the robustness of learning-based methods in real-world scenes.

2) *Memory Consumption and Run-time*: Low run-time and memory consumption are essential in most industrial applications with limited computational power and storage, e.g., autonomous driving and AR/VR. Because of the low-

TABLE IV

QUANTITATIVE RESULTS OF POINT CLOUD EVALUATION ON MVS BENCHMARKS [21]–[23] FOR SUPERVISED OFFLINE MVS METHODS. “FINETUNED WITH BLENDEDMVS” DENOTES WHETHER THE LEARNING-BASED METHODS ARE FINETUNED ON BLENDEDMVS [24] BEFORE EVALUATING ON TANKS AND TEMPLES [22] AND ETH3D [23].

Methods		DTU [21]			Finetuned with BlendedMVS [24]	Tanks and Temples [22]		ETH3D [23]	
		Acc. ↓	Comp. ↓	Overall ↓		Intermediate F_1 ↑	Advanced F_1 ↑	Training F_1 ↑	Test F_1 ↑
Direct 3D CNN	MVSNet [15]	0.396	0.527	0.462	✗	43.48	-	-	-
	P-MVSNet [182]	0.406	0.434	0.420	✗	55.62	-	-	-
	CIDER [36]	0.417	0.437	0.427	✗	46.76	23.12	-	-
	PointMVSNet [95]	0.342	0.411	0.376	-	-	-	-	-
	VA-Point-MVSNet [116]	0.359	0.358	0.359	✗	48.70	-	-	-
	PVA-MVSNet [90]	0.379	0.336	0.357	✗	54.46	-	-	-
	Fast-MVSNet [117]	0.336	0.403	0.370	✗	47.39	-	-	-
RNN	R-MVSNet [37]	0.383	0.452	0.417	✗	48.40	24.91	-	-
	D^2 HC-RMVSNet [38]	0.395	0.378	0.386	✗	59.20	-	-	-
	AA-RMVSNet [77]	0.376	0.339	0.357	✓	61.51	-	-	-
	BH-RMVSNet [183]	0.368	0.303	0.335	✓	61.96	34.81	-	79.61
Coarse-to-fine	CasMVSNet [32]	0.325	0.385	0.355	✗	56.84	-	-	-
	CVP-MVSNet [75]	0.296	0.406	0.351	✗	54.03	-	-	-
	UCS-Net [39]	0.338	0.349	0.344	✗	54.83	-	-	-
	AttMVS [184]	0.383	0.329	0.356	✗	60.05	37.34	-	-
	Vis-MVSNet [92]	0.369	0.361	0.365	✓	60.03	-	-	-
	EPP-MVSNet [100]	0.413	0.296	0.355	✓	61.68	35.72	74.00	83.40
	CDS-MVSNet [80]	0.351	0.278	0.315	✓	61.58	-	-	-
	TransMVSNet [79]	0.321	0.289	0.305	✓	63.52	37.00	-	-
	GBi-Net [78]	0.315	0.262	0.289	✓	61.42	37.32	-	-
	UniMVSNet [114]	0.352	0.278	0.315	✓	64.36	38.96	-	-
	NP-CVP-MVSNet [185]	0.356	0.275	0.315	✓	59.64	-	-	-
	MVSTER [99]	0.340	0.266	0.303	✓	60.92	37.53	72.06	79.01
	PVSNet [63]	0.337	0.315	0.326	✓	59.11	35.51	76.57	82.62
	MVSFormer [82]	0.327	0.251	0.289	✓	66.37	40.87	-	-
	IS-MVSNet [186]	0.351	0.359	0.355	✓	62.82	34.87	73.33	83.15
	HR-MVSNet [187]	0.332	0.310	0.321	✓	63.12	34.27	-	-
	EPNet [121]	0.299	0.323	0.313	✓	63.68	40.52	79.08	83.72
	GeoMVSNet [76]	0.331	0.259	0.295	✓	65.89	41.52	-	-
RA-MVSNet [188]	0.326	0.268	0.297	✓	65.72	39.93	-	-	
DMVSNet [115]	0.338	0.272	0.305	✓	64.66	41.17	-	-	
ET-MVSNet [86]	0.329	0.253	0.291	✓	65.49	40.41	-	-	
Iterative update	PatchmatchNet [40]	0.427	0.277	0.352	✗	53.15	32.31	64.21	73.12
	PatchMatch-RL [103]	-	-	-	✓	51.80	31.80	67.80	72.40
	IterMVS [41]	0.373	0.354	0.363	✓	56.94	34.17	71.69	80.09
	Effi-MVS [102]	0.321	0.313	0.317	✗	56.88	34.39	-	-
	CER-MVS [101]	0.359	0.305	0.332	✓	64.82	40.19	-	-
	IGEV-MVS [112]	0.331	0.326	0.324	-	-	-	-	-

resolution input and the simplicity of network structures, online MVS methods [25], [31], [35] usually achieve high efficiency in both memory and run-time. In contrast, offline MVS methods focus on high-resolution images and usually use computationally expensive network modules, *e.g.*, 3D convolutions, to improve reconstruction quality. These increase run-time and GPU memory. Recently, many researchers try to improve the efficiency while maintaining the reconstruction accuracy as other offline MVS methods. We compare and summarize the efficiency of existing efficient methods [32], [39]–[41], [99], [102], [117] in Fig. 13. All the methods share similar coarse-to-fine structures to improve efficiency. To further reduce run-time and memory, [40], [41], [99],

[102] further get rid of costly 3D convolution and use 2D convolution instead. It can be found many methods [40], [41], [99], [102] can achieve near real-time estimation (about 10 Hz) with relatively high resolution images, *e.g.*, 1152×864 . In conclusion, it is promising to further improve both the performance and efficiency for practical applications.

C. Unsupervised MVS with Depth Estimation

We summarize the results of unsupervised MVS methods in Tab. III. Based on the conventional photometric consistency loss (Sec. III-A), unsupervised MVS methods may have difficulties with many challenging situations, *e.g.*, varying lighting conditions or occlusions, and suffer from downgraded recon-

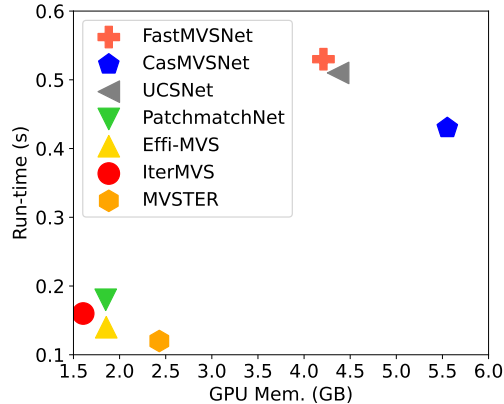


Fig. 13. GPU memory consumption and run-time of efficient offline methods [32], [39]–[41], [99], [102], [117] on DTU dataset [21]. The image resolution and the number of images are set to 1152×864 and 5 respectively. Experiments are done on a NVIDIA 2080Ti GPU.

struction results. Therefore, many methods propose to employ different strategies to improve the robustness, *e.g.*, segmentation consistency [42], optical flow consistency [44], neural rendering consistency [43], pseudo-label generation with geometric filtering [45], [132], multi-iteration training [45], [132] and featuremetric loss [45]. It is inspiring that KD-MVS [45] already outperforms its backbone, CasMVSNet [32], and many other fully supervised methods. However, since unsupervised methods mainly test on relatively simple scenes [21], [22], their scalability to more complex and large-scale scenes, *e.g.*, ETH3D [23], remains a question. This good generalization capability across various scenes and datasets is crucial for practical applications. Therefore, evaluating unsupervised MVS methods on various scenes is an important task for future research. Most unsupervised methods use simple MVS backbones [15], [32], [75] and mainly focus on the training strategy. Employing state-of-the-art architectures is also a potential direction that can further boost the performance.

D. Learning-based MVS without Depth Estimation

1) *Voxel-based Methods*: We summarize the quantitative results on ScanNet [26] in Tab. V. Since the voxel representation increases the computation overhead explicitly when the scale of scene increases, voxel-based methods mainly focus on indoor scenes, *e.g.*, ScanNet [26]. We find that depth map-based MVS methods, *e.g.*, SimpleRecon [35], fuse depth maps with traditional TSDF fusion [64] and can achieve comparable performance as these voxel-based methods with lower complexity. This further shows the advantages of depth map-based methods over voxel-based methods.

2) *NeRF-based Methods*: The quantitative results of nerf-based methods on DTU dataset [21] are summarized in Tab. VI. We visualize the qualitative reconstructions of two representative methods, NeuS [50] and VolSDF [49], in Fig. 14. The most outstanding features of NeuS [50] and VolSDF [49] are that they are self-supervised, *i.e.*, without depth supervision, and produce smooth and complete mesh surfaces. However, many recent methods [154]–[156] find that

TABLE V
QUANTITATIVE RESULTS OF VOXEL-BASED MVS METHODS ON SCANNET [26].

Methods	Prec. \uparrow	Recall \uparrow	F-score \uparrow
Atlas [47]	0.675	0.605	0.636
NeuralRecon [48]	0.630	0.612	0.619
TransformerFusion [142]	0.728	0.600	0.655
VoRTX [143]	0.767	0.651	0.703

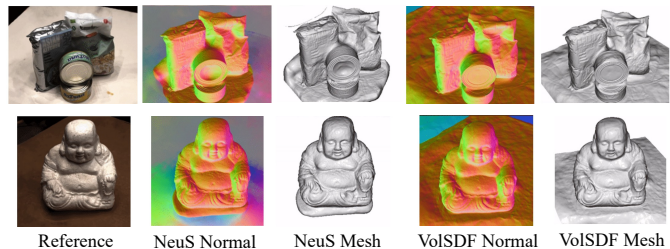


Fig. 14. Reconstruction results (rendered surface normal map and surface mesh) of NeuS [50] and VolSDF [49] on DTU dataset [21]. NeuS and VolSDF apply different approximation of density with SDF.

incorporating more explicit geometric supervision explicitly improves the reconstruction quality. Compared with depth map-based MVS methods [15], [25], the main drawback of NeRF-based methods is that they are mostly per-scene optimization problems and need lots of time to train the model on each new scene. Recently, some methods [161]–[163] try to make the pipeline generalizable so that there is no need to train the model for new scenes. However, they perform worse than depth map-based methods [15]. Another way to improve training time efficiency is to employ hash grids [146], which also improves surface details. However, these methods [157]–[160] need lots of GPU memory and space to train and store the large model. In addition, the scalability of NeRF-based methods remains a problem when attempting to apply on large-scale scenes [23].

3) *3D Gaussian Splatting-based Methods*: Because of its highly efficient rasterization, 3D Gaussian Splatting [170] becomes popular in novel view synthesis and gradually replaces NeRF [28] in the last half year. Recently, some researchers start exploring the potential of 3D Gaussian Splatting in surface reconstruction. However, there are many challenges. For example, the 3D Gaussians do not correspond well to the actual surface of the scene since the 3D Gaussian has a 3D covariance matrix [52]. Moreover, the surface may contain noisy undulations [52]. However, it is worthwhile to further explore in this direction since 3D Gaussian Splatting is much faster to train than those NeRF-based MVS methods. Moreover, instead of directly extracting the surface from 3D space [52], rendering accurate depth maps and then fuse them like depth map-based MVS methods is a potential direction.

4) *Large Feed-forward Methods*: As a new trend of 3D reconstruction, large feed-forward methods demonstrate their impressive performance in challenging settings that other MVS methods cannot handle, *e.g.*, single image input and un-posed sparse images. Employing a large model that is able to get

TABLE VI
QUANTITATIVE RESULTS OF NERF-BASED MVS METHODS ON DTU [21].

Methods	VolSDF [49]	NeuS [50]	NeuralWarp [133]	HF-NeuS [190]	RegSDF [191]	PET-NeuS [192]
Overall ↓	0.86	0.87	0.68	0.77	0.72	0.71
Methods	GeoNeuS [156]	Voxurf [193]	NeuS2 [157]	PermutoSDF [159]	Neuralangelo [158]	UniSDF [160]
Overall ↓	0.51	0.72	0.70	0.68	0.61	0.64

scaled up, these methods manage to learn strong priors of multi-view geometry from large datasets [30]. However, these methods [53], [54], [179] face limitations when it comes to extending the scale of the scene. For example, the 3D representation employed in LRM [53] is a tri-plane representation [180], which has a small resolution and struggles with scaling to larger sizes due to memory constraints. In addition, the tri-plane representation is difficult to model more complex geometry, *e.g.*, with strong self-occlusions. In addition to tri-plane-based 3D representations, new methods [194], [195] have been proposed that directly reconstruct 3D Gaussians in a feed-forward manner. These new methods demonstrate improved capabilities in reconstructing both objects and scenes, but require posed sparse images as inputs. It is worth noting that the generalization ability of these methods is questionable since they learn priors of multi-view geometry completely from the training dataset, while the depth map-based methods utilize feature matching from plane sweep algorithm from traditional methods. Moreover, these methods typically need high-end GPUs since they are usually GPU memory consuming. It is worth noting that, since large feed-forward methods usually do not enforce geometric constraint explicitly, *e.g.*, epipolar geometry, the reconstructed geometry is by default placed in a local coordinate system without absolute scales, making it not feasible for applications requiring precise measurement.

E. Future Research Directions

1) *Datasets and Benchmarks:* For learning-based MVS methods, ScanNet [26] and DTU [21] are two main training datasets, while ScanNet [26], DTU [21], Tanks & Temples [22] and ETH3D [23] are the main evaluation benchmarks.

For training, the scene scale of ScanNet and DTU is relatively small (room-scale for ScanNet and object-scale for DTU) and their quality is not satisfactory. For example, the camera calibration of ScanNet is not very accurate. For DTU, the ground truth depth maps are rendered from mesh, which contain some outliers and holes. This is because the mesh is reconstructed from the sparse ground truth point cloud with Screened Poisson surface reconstruction [67] and thus contains incomplete regions [184]. Therefore, improving the scalability and quality of training datasets is an important research direction.

Recently, there are many researchers trying to solve this problem. TartanAir dataset [196] is a large-scale synthetic dataset that is collected in photo-realistic simulation environments. Precise multi-modal sensor data and ground truth labels are provided, including the stereo RGB image, depth image, segmentation, optical flow, camera poses, and LiDAR point

cloud. BlendedMVS [24] introduces more large-scale scenes and improves the performance of many MVS methods on real-world scenes, shown in Tab. IV. ArKitScenes [197] consists of 5,048 RGB-D sequences, which is more than three times the size of the current largest available indoor dataset, ScanNet. As an extension of ScanNet, ScanNet++ [198] is a large-scale dataset that captures high-quality geometry and color of indoor scenes with high-end laser scanner, DSLR camera, and RGB-D streams from an iPhone. Motivated by ImageNet [199] that drives a remarkable trend of learning from large-scale data in 2D visual tasks, Yu *et al.* [200] propose MVImgNet, a large-scale dataset of multi-view images collected by shooting videos of real-world objects. MVImgNet demonstrates the potential of various 3D visual tasks, including radiance field reconstruction, multi-view stereo, and view-consistent image understanding. Similarly, Objaverse [30] is a large dataset of objects with 800K+ (and growing) 3D models with descriptive captions, tags, and animations. Both MVImgNet [199] and Objaverse [30] can be used to train large feed-forward models, *e.g.*, LRM [53], for reconstruction, since these models need massive data to learn the strong prior. However, both of them mainly focus on object-level scenes. Large datasets for larger-scale scenes, *e.g.*, rooms, are valuable to be explored.

For evaluation, the main benchmarks [21]–[23], [26] are all introduced before 2018. Some of these benchmarks, *e.g.*, [21], [22], are currently saturated and the learning-based methods are difficult to further improve the performance on them. Therefore, it is meaningful to introduce new benchmarks to evaluate the robustness and performance of learning-based methods in challenging real-world scenes. For example, LaMAR [201] is a recent large-scale dataset captured using multiple modern AR devices in diverse environments. It contains challenging short-term appearance and structural changes and high quality LiDAR point cloud ground truth. These make LaMAR a potential benchmark for MVS.

2) *View Selection:* As discussed in Sec. I-B, view selection is crucial for triangulation quality. Picking neighboring views that are suitable for triangulation can not only improve the reconstruction accuracy but also reduce useless computation for the bad views, *e.g.*, views with strong occlusions. However, view selection is often overlooked and not well studied. For example, all offline depth map-based MVS methods [32], [40], [79], [99] follow MVSNet [15] and use the same simple heuristic strategy to compute scores for neighboring views and sort them. Online depth map-based MVS methods [31], [35], [58] and voxel-based methods [48] also adopt heuristic strategies to choose views with enough pose-distance. Though it is intractable to incorporate non-differentiable view selection

into deep learning, it is worth exploring new view selection strategies since it may improve the reconstruction without changing the model design of existing methods. Current view selection strategies simply pick the same set of neighboring views for all the pixels in the reference image, and it is probable that different reference pixels have different optimal choices of neighboring views. If it is possible to choose the best neighboring views for each pixel, reconstruction quality can be further improved and computation reduced. The learned pixel-wise view weight [40], [41], [63] is one solution for this since it weights the source views differently for each pixel based on its visibility across neighboring views.

3) *Depth Fusion*: As discussed in Sec. I-D, both online and offline MVS methods with plane-sweep use traditional TSDF fusion or depth filtering methods to reconstruct mesh or point cloud from the estimated depth maps. However, TSDF fusion [64], [65] is not robust enough to the outliers in the depth maps and may have memory issues due to the dense volumetric representation. Depth filtering following Galliani *et al.* [18] introduces lots of hyper-parameters. Researchers may carefully finetune these hyper-parameters for each scene since it may have a great impact on the evaluation metrics. Therefore, it is valuable to improve the depth fusion step so that the reconstruction quality can be further improved. Recently, there have been some learning-based depth map fusion methods [202], [203]. However, they are limited to small scenes due to the dense volume representation and large memory consumption.

4) *Features*: One not well-studied topic is what kind of feature extractors are suitable for MVS, as mentioned in Sec. II-A. So far, most of the offline depth map-based methods [15], [32], [78] mainly apply simple 2D CNN and FPN [72] structure as a feature extractor. To improve the receptive fields flexibly, Deformation Convolution [204] is used [40], [77]–[79]). The attention mechanism is also applied in feature learning, where works such as [77], [79], [90] use intra-attention or inter-attention to capture long-range feature dependencies. Furthermore, MVFormer [82] digs deeper into using patch-wise ViT [181] as a feature extractor in MVS. The insight is that ViT works better to formulate global feature correlations, and FPN can learn detailed ones. In contrast, online depth map-based methods [31], [35] usually adopt efficient pretrained backbones [70], [73], [74]. Recently, large feed-forward methods [53], [54], [175] adopt large pretrained feature encoders, *e.g.*, ViT [181], DINO [83], to learn strong prior from large-amount of data. However, using a powerful feature extraction network usually increases the computation overhead and reduces the efficiency. Finding a good balance between performance and efficiency is an interesting direction, *e.g.*, distilling the large ViT into a relatively small transformer [205].

5) *Real-time and Memory Efficient Models*: Though reconstruction accuracy is considered the most important factor in MVS, it is also critical to have models that can run in near real-time and with low memory, *e.g.*, AR/VR and autonomous driving. Comparatively, depth map-based methods are most suitable for achieving efficiency because of their conciseness, flexibility, and scalability. Though online MVS methods can

achieve real-time estimation with images of low resolutions, they may have issues with memory consumption since many large backbones are usually used for feature extraction [31], [35]. In addition, the efficiency in both run-time and memory will drop when image resolution increases. For offline MVS methods, as discussed in Sec. V-B2, some recent methods try to improve efficiency with carefully simplified network architectures. However, this usually limits the performance when compared with state-of-the-art methods. There are many other directions for further improvement. For example, using model compression techniques and knowledge distillation are potential directions to not only keep the good performance and also improve efficiency.

6) *Prior Assistance*: MVS mainly relies on measurements of local photometric consistency to find the optimal matching across reference and source images. Accordingly, it usually encounters difficulties when estimating the geometry for regions where the photometric measurement becomes unreliable or invalid, *e.g.*, textureless areas and non-Lambertian surfaces, which are common in human-made environments, *e.g.*, ETH3D [23]. Therefore, leveraging prior information to guide the MVS algorithm in these challenging regions is a promising research direction. We elaborate several typical examples of prior assistance as follows.

- **Surface Normal**: It is a non-local representation of the geometry compared with the depth map. To enforce the constraints of normal maps in depth estimation, Kusupati *et al.* [206] integrate the multi-view normal estimation network into the MVS pipeline. Long *et al.* [207] introduce a Combined Normal Map, estimated with PlaneCNN [208] to enforce the normal consistency on the depth map. Liu *et al.* [209] perform graph-based depth map optimization as post-processing. Since normal monocular normal predictions [210] provide high-quality priors for the full scene, [154], [155] use monocular normal to improve the optimization of neural implicit surfaces.
- **Shape Prior**: For indoor scenes where common textureless areas, *e.g.*, walls, planes are suitable choices of the geometric primitives and are exploited in traditional methods [20]. Recently, PlaneMVS [211] and PlanarRecon [212] explicitly estimate plane parameters for depth refinement or holistic reconstruction. In addition, predicting object-level attributes simultaneously when estimating depth [213] is also a feasible solution for specific applications like urban modeling.
- **Semantic Segmentation**: Intuitively, points assigned with the same semantic labels may be more likely to lie on the same 3D plane. Some attempts [214], [215] employ a rule-based protocol to utilize semantic segmentation for better matching and depth quality. Manhattan-SDF [216] adopts Manhattan world priors to handle low-textured planar regions corresponding to walls and floors with 2D segmentation.

VI. CONCLUSION

In this survey, we have provided a comprehensive review of the learning-based MVS methods until 2023, which

are categorized into: depth map-based, voxel-based, NeRF-based, 3D Gaussian Splatting-based and large feed-forward methods. Particularly, we have devoted significant attention to depth map-based methods because of their conciseness, flexibility and scalability. We explain key aspects such as datasets utilized, general working pipelines, and algorithmic intricacies. Furthermore, we have summarized and compared the quantitative performance of these methods across popular benchmarks, providing valuable insights into their efficacy and applicability. Finally, our discourse extends to an in-depth exploration of potential research directions for the future of MVS, highlighting avenues for further investigation and innovation in the field.

REFERENCES

- [1] Y. Furukawa and C. Hernández, “Multi-view stereo: A tutorial,” *Foundations and Trends® in Computer Graphics and Vision*, vol. 9, no. 1-2, 2015.
- [2] J. Sturm, N. Engelhard, F. Endres, W. Burgard, and D. Cremers, “A benchmark for the evaluation of rgb-d slam systems,” in *IROS*, 2012.
- [3] F. Endres, J. Hess, J. Sturm, D. Cremers, and W. Burgard, “3-d mapping with an rgb-d camera,” *IEEE transactions on robotics*, vol. 30, no. 1, pp. 177–187, 2013.
- [4] T. Schops, T. Sattler, and M. Pollefeys, “Bad slam: Bundle adjusted direct rgb-d slam,” in *CVPR*, 2019.
- [5] Y. Pan, P. Xiao, Y. He, Z. Shao, and Z. Li, “Mulls: Versatile lidar slam via multi-metric linear least square,” in *ICRA*, 2021.
- [6] S. Izadi, D. Kim, O. Hilliges, D. Molyneaux, R. Newcombe, P. Kohli, J. Shotton, S. Hodges, D. Freeman, A. Davison *et al.*, “Kinectfusion: real-time 3d reconstruction and interaction using a moving depth camera,” in *Proceedings of the 24th annual ACM symposium on User interface software and technology*, 2011.
- [7] M. Zollhöfer, M. Nießner, S. Izadi, C. Rehmann, C. Zach, M. Fisher, C. Wu, A. Fitzgibbon, C. Loop, C. Theobalt *et al.*, “Real-time non-rigid reconstruction using an rgb-d camera,” *ACM Transactions on Graphics (ToG)*, vol. 33, no. 4, 2014.
- [8] R. A. Newcombe, D. Fox, and S. M. Seitz, “Dynamicfusion: Reconstruction and tracking of non-rigid scenes in real-time,” in *CVPR*, 2015.
- [9] S. M. Seitz and C. R. Dyer, “Photorealistic scene reconstruction by voxel coloring,” *IJCV*, vol. 35, 1999.
- [10] K. N. Kutulakos and S. M. Seitz, “A theory of shape by space carving,” *IJCV*, vol. 38, 2000.
- [11] I. Kostrikov, E. Horbert, and B. Leibe, “Probabilistic labeling cost for high-accuracy multi-view reconstruction,” in *CVPR*, 2014.
- [12] A. O. Ulusoy, M. J. Black, and A. Geiger, “Semantic multi-view stereo: Jointly estimating objects and voxels,” in *CVPR*, 2017.
- [13] M. Lhuillier and L. Quan, “A quasi-dense approach to surface reconstruction from uncalibrated images,” *IEEE transactions on pattern analysis and machine intelligence*, vol. 27, no. 3, 2005.
- [14] Y. Furukawa and J. Ponce, “Accurate, dense, and robust multiview stereopsis,” *IEEE transactions on pattern analysis and machine intelligence*, vol. 32, no. 8, 2009.
- [15] Y. Yao, Z. Luo, S. Li, T. Fang, and L. Quan, “Mvsnet: Depth inference for unstructured multi-view stereo,” in *ECCV*, 2018.
- [16] R. Yang and M. Pollefeys, “Multi-resolution real-time stereo on commodity graphics hardware,” in *CVPR*, 2003.
- [17] J. L. Schönberger and J.-M. Frahm, “Structure-from-motion revisited,” in *CVPR*, 2016.
- [18] S. Galliani, K. Lasinger, and K. Schindler, “Massively parallel multi-view stereopsis by surface normal diffusion,” in *ICCV*, 2015.
- [19] Q. Xu and W. Tao, “Multi-scale geometric consistency guided multi-view stereo,” in *CVPR*, 2019.
- [20] —, “Planar prior assisted patchmatch multi-view stereo,” in *AAAI*, 2020.
- [21] H. Aanæs, R. R. Jensen, G. Vogiatzis, E. Tola, and A. B. Dahl, “Large-scale data for multiple-view stereopsis,” *IJCV*, vol. 120, no. 2, pp. 153–168, 2016.
- [22] A. Knapitsch, J. Park, Q.-Y. Zhou, and V. Koltun, “Tanks and temples: Benchmarking large-scale scene reconstruction,” *ACM Transactions on Graphics (ToG)*, vol. 36, no. 4, pp. 1–13, 2017.
- [23] T. Schöps, J. L. Schönberger, S. Galliani, T. Sattler, K. Schindler, M. Pollefeys, and A. Geiger, “A multi-view stereo benchmark with high-resolution images and multi-camera videos,” in *CVPR*, 2017.
- [24] Y. Yao, Z. Luo, S. Li, J. Zhang, Y. Ren, L. Zhou, T. Fang, and L. Quan, “Blendedmvs: A large-scale dataset for generalized multi-view stereo networks,” in *CVPR*, 2020.
- [25] K. Wang and S. Shen, “Mvdepthnet: Real-time multiview depth estimation neural network,” in *3DV*, 2018.
- [26] A. Dai, A. X. Chang, M. Savva, M. Halber, T. Funkhouser, and M. Nießner, “ScanNet: Richly-annotated 3d reconstructions of indoor scenes,” in *CVPR*, 2017.
- [27] B. Glocker, S. Izadi, J. Shotton, and A. Criminisi, “Real-time rgb-d camera relocation,” in *2013 IEEE International Symposium on Mixed and Augmented Reality (ISMAR)*. IEEE, 2013.
- [28] B. Mildenhall, P. P. Srinivasan, M. Tancik, J. T. Barron, R. Ramamoorthi, and R. Ng, “Nerf: Representing scenes as neural radiance fields for view synthesis,” in *ECCV*, 2020.
- [29] B. Kerbl, G. Kopanas, T. Leimkühler, and G. Drettakis, “3d gaussian splatting for real-time radiance field rendering,” *ACM Transactions on Graphics*, vol. 42, no. 4, 2023.
- [30] M. Deitke, D. Schwenk, J. Salvador, L. Weihs, O. Michel, E. VanderBilt, L. Schmidt, K. Ehsani, A. Kembhavi, and A. Farhadi, “Objaverse: A universe of annotated 3d objects,” in *CVPR*, 2023.
- [31] A. Duzceker, S. Galliani, C. Vogel, P. Speciale, M. Dusmanu, and M. Pollefeys, “Deepvideomvs: Multi-view stereo on video with recurrent spatio-temporal fusion,” in *CVPR*, 2021.
- [32] X. Gu, Z. Fan, S. Zhu, Z. Dai, F. Tan, and P. Tan, “Cascade cost volume for high-resolution multi-view stereo and stereo matching,” in *CVPR*, 2020.
- [33] R. T. Collins, “A space-sweep approach to true multi-image matching,” in *CVPR*, 1996.
- [34] J. L. Schönberger, E. Zheng, J.-M. Frahm, and M. Pollefeys, “Pixelwise view selection for unstructured multi-view stereo,” in *ECCV*, 2016.
- [35] M. Sayed, J. Gibson, J. Watson, V. Prisacariu, M. Firman, and C. Godard, “Simplerecon: 3d reconstruction without 3d convolutions,” in *ECCV*. Springer, 2022, pp. 1–19.
- [36] Q. Xu and W. Tao, “Learning inverse depth regression for multi-view stereo with correlation cost volume,” in *AAAI*, 2020.
- [37] Y. Yao, Z. Luo, S. Li, T. Shen, T. Fang, and L. Quan, “Recurrent mvsnet for high-resolution multi-view stereo depth inference,” in *CVPR*, 2019.
- [38] J. Yan, Z. Wei, H. Yi, M. Ding, R. Zhang, Y. Chen, G. Wang, and Y.-W. Tai, “Dense hybrid recurrent multi-view stereo net with dynamic consistency checking,” in *ECCV*, 2020.
- [39] S. Cheng, Z. Xu, S. Zhu, Z. Li, L. E. Li, R. Ramamoorthi, and H. Su, “Deep stereo using adaptive thin volume representation with uncertainty awareness,” in *CVPR*, 2020.
- [40] F. Wang, S. Galliani, C. Vogel, P. Speciale, and M. Pollefeys, “Patchmatchnet: Learned multi-view patchmatch stereo,” in *CVPR*, 2021.
- [41] F. Wang, S. Galliani, C. Vogel, and M. Pollefeys, “Itermvs: Iterative probability estimation for efficient multi-view stereo,” 2022.
- [42] H. Xu, Z. Zhou, Y. Qiao, W. Kang, and Q. Wu, “Self-supervised multi-view stereo via effective co-segmentation and data-augmentation,” in *AAAI*, 2021.
- [43] D. Chang, A. Božič, T. Zhang, Q. Yan, Y. Chen, S. Süssstrunk, and M. Nießner, “Rc-mvsnet: unsupervised multi-view stereo with neural rendering,” in *ECCV*, 2022.
- [44] H. Xu, Z. Zhou, Y. Wang, W. Kang, B. Sun, H. Li, and Y. Qiao, “Digging into uncertainty in self-supervised multi-view stereo,” in *ICCV*, 2021.
- [45] Y. Ding, Q. Zhu, X. Liu, W. Yuan, H. Zhang, and C. Zhang, “Kd-mvs: Knowledge distillation based self-supervised learning for multi-view stereo,” in *ECCV*, 2022.
- [46] T. Kim, J. Choi, S. Choi, D. Jung, and C. Kim, “Just a few points are all you need for multi-view stereo: A novel semi-supervised learning method for multi-view stereo,” in *ICCV*, 2021.
- [47] Z. Murez, T. v. As, J. Bartolozzi, A. Sinha, V. Badrinarayanan, and A. Rabinovich, “Atlas: End-to-end 3d scene reconstruction from posed images,” in *ECCV*, 2020.
- [48] J. Sun, Y. Xie, L. Chen, X. Zhou, and H. Bao, “Neuralrecon: Real-time coherent 3d reconstruction from monocular video,” in *CVPR*, 2021.
- [49] L. Yariv, J. Gu, Y. Kasten, and Y. Lipman, “Volume rendering of neural implicit surfaces,” in *Advances in Neural Information Processing Systems*, 2021.
- [50] P. Wang, L. Liu, Y. Liu, C. Theobalt, T. Komura, and W. Wang, “Neus: Learning neural implicit surfaces by volume rendering for multi-view reconstruction,” in *Advances in Neural Information Processing Systems*, 2021.

- [51] J. Tang, J. Ren, H. Zhou, Z. Liu, and G. Zeng, "Dreamgaussian: Generative gaussian splatting for efficient 3d content creation," *arXiv preprint arXiv:2309.16653*, 2023.
- [52] A. Guédon and V. Lepetit, "Sugar: Surface-aligned gaussian splatting for efficient 3d mesh reconstruction and high-quality mesh rendering," in *CVPR*, 2024.
- [53] Y. Hong, K. Zhang, J. Gu, S. Bi, Y. Zhou, D. Liu, F. Liu, K. Sunkavalli, T. Bui, and H. Tan, "Lrm: Large reconstruction model for single image to 3d," *ICLR*, 2024.
- [54] S. Wang, V. Leroy, Y. Cabon, B. Chidlovskii, and J. Revaud, "Dust3r: Geometric 3d vision made easy," in *CVPR*, 2024.
- [55] R. Hartley and A. Zisserman, *Multiple view geometry in computer vision*. Cambridge university press, 2003.
- [56] P. Moulon, P. Monasse, R. Perrot, and R. Marlet, "Openmvg: Open multiple view geometry," in *International Workshop on Reproducible Research in Pattern Recognition*, 2016.
- [57] A. Dai, M. Nießner, M. Zollhöfer, S. Izadi, and C. Theobalt, "Bundlefusion: Real-time globally consistent 3d reconstruction using on-the-fly surface reintegration," *ACM Transactions on Graphics (ToG)*, vol. 36, no. 4, p. 1, 2017.
- [58] Y. Hou, J. Kannala, and A. Solin, "Multi-view stereo by temporal nonparametric fusion," in *ICCV*, 2019.
- [59] R. Zhang, S. Li, T. Fang, S. Zhu, and L. Quan, "Joint camera clustering and surface segmentation for large-scale multi-view stereo," in *ICCV*, 2015.
- [60] A. Kendall, H. Martirosyan, S. Dasgupta, P. Henry, R. Kennedy, A. Bachrach, and A. Bry, "End-to-end learning of geometry and context for deep stereo regression," in *ICCV*, 2017.
- [61] J.-R. Chang and Y.-S. Chen, "Pyramid stereo matching network," in *CVPR*, 2018.
- [62] X. Guo, K. Yang, W. Yang, X. Wang, and H. Li, "Group-wise correlation stereo network," in *CVPR*, 2019.
- [63] Q. Xu, W. Su, Y. Qi, W. Tao, and M. Pollefeys, "Learning inverse depth regression for pixelwise visibility-aware multi-view stereo networks," *IJCV*, vol. 130, no. 8, pp. 2040–2059, 2022.
- [64] B. Curless and M. Levoy, "A volumetric method for building complex models from range images," in *Proceedings of the 23rd annual conference on Computer graphics and interactive techniques*, 1996.
- [65] R. A. Newcombe, S. Izadi, O. Hilliges, D. Molyneaux, D. Kim, A. J. Davison, P. Kohi, J. Shotton, S. Hodges, and A. Fitzgibbon, "Kinectfusion: Real-time dense surface mapping and tracking," in *2011 10th IEEE international symposium on mixed and augmented reality*, 2011.
- [66] W. E. Lorensen and H. E. Cline, "Marching cubes: A high resolution 3d surface construction algorithm," in *Seminal graphics: pioneering efforts that shaped the field*, 1998, pp. 347–353.
- [67] M. Kazhdan and H. Hoppe, "Screened poisson surface reconstruction," *ACM Transactions on Graphics (ToG)*, vol. 32, no. 3, pp. 1–13, 2013.
- [68] D. Eigen, C. Puhrsch, and R. Fergus, "Depth map prediction from a single image using a multi-scale deep network," *Advances in neural information processing systems*, 2014.
- [69] A. Sinha, Z. Murez, J. Bartolozzi, V. Badrinarayanan, and A. Rabinovich, "Deltas: Depth estimation by learning triangulation and densification of sparse points," in *ECCV*, 2020.
- [70] K. He, X. Zhang, S. Ren, and J. Sun, "Deep residual learning for image recognition," in *CVPR*, 2016.
- [71] O. Ronneberger, P. Fischer, and T. Brox, "U-net: Convolutional networks for biomedical image segmentation," in *International Conference on Medical image computing and computer-assisted intervention*, 2015.
- [72] T.-Y. Lin, P. Dollár, R. B. Girshick, K. He, B. Hariharan, and S. J. Belongie, "Feature pyramid networks for object detection," *CVPR*, 2017.
- [73] M. Tan, B. Chen, R. Pang, V. Vasudevan, M. Sandler, A. Howard, and Q. V. Le, "Mnasnet: Platform-aware neural architecture search for mobile," in *CVPR*, 2019, pp. 2820–2828.
- [74] M. Tan and Q. Le, "Efficientnetv2: Smaller models and faster training," in *ICML*. PMLR, 2021, pp. 10 096–10 106.
- [75] J. Yang, W. Mao, J. M. Alvarez, and M. Liu, "Cost volume pyramid based depth inference for multi-view stereo," in *CVPR*, 2020.
- [76] Z. Zhang, R. Peng, Y. Hu, and R. Wang, "Geomvsnet: Learning multi-view stereo with geometry perception," in *CVPR (CVPR)*, June 2023, pp. 21 508–21 518.
- [77] Z. Wei, Q. Zhu, C. Min, Y. Chen, and G. Wang, "Aa-rmvsnet: Adaptive aggregation recurrent multi-view stereo network," in *ICCV*, 2021.
- [78] Z. Mi, D. Chang, and D. Xu, "Generalized binary search network for highly-efficient multi-view stereo," in *CVPR*, 2022.
- [79] Y. Ding, W. Yuan, Q. Zhu, H. Zhang, X. Liu, Y. Wang, and X. Liu, "Transmvsnet: Global context-aware multi-view stereo network with transformers," *arXiv preprint arXiv:2111.14600*, 2021.
- [80] K. T. Giang, S. Song, and S. Jo, "Curvature-guided dynamic scale networks for multi-view stereo," *arXiv preprint arXiv:2112.05999*, 2021.
- [81] J. Liao, Y. Ding, Y. Shavit, D. Huang, S. Ren, J. Guo, W. Feng, and K. Zhang, "Wt-mvsnet: window-based transformers for multi-view stereo," *Advances in Neural Information Processing Systems*, 2022.
- [82] C. Cao, X. Ren, and Y. Fu, "Mvsformer: Learning robust image representations via transformers and temperature-based depth for multi-view stereo," *arXiv preprint arXiv:2208.02541*, 2022.
- [83] M. Caron, H. Touvron, I. Misra, H. Jégou, J. Mairal, P. Bojanowski, and A. Joulin, "Emerging properties in self-supervised vision transformers," in *ICCV*, 2021, pp. 9650–9660.
- [84] X. Chu, Z. Tian, Y. Wang, B. Zhang, H. Ren, X. Wei, H. Xia, and C. Shen, "Twins: Revisiting the design of spatial attention in vision transformers," *Advances in Neural Information Processing Systems*, vol. 34, pp. 9355–9366, 2021.
- [85] Z. Liu, Y. Lin, Y. Cao, H. Hu, Y. Wei, Z. Zhang, S. Lin, and B. Guo, "Swin transformer: Hierarchical vision transformer using shifted windows," in *ICCV*, 2021.
- [86] T. Liu, X. Ye, W. Zhao, Z. Pan, M. Shi, and Z. Cao, "When epipolar constraint meets non-local operators in multi-view stereo," in *ICCV*, 2023.
- [87] C. Liu, J. Gu, K. Kim, S. G. Narasimhan, and J. Kautz, "Neural rgb (r) d sensing: Depth and uncertainty from a video camera," in *CVPR*, 2019.
- [88] G. Bae, I. Budvytis, and R. Cipolla, "Multi-view depth estimation by fusing single-view depth probability with multi-view geometry," in *CVPR*, 2022.
- [89] X. Guo, K. Yang, W. Yang, X. Wang, and H. Li, "Group-wise correlation stereo network," in *CVPR*, 2019.
- [90] H. Yi, Z. Wei, M. Ding, R. Zhang, Y. Chen, G. Wang, and Y.-W. Tai, "Pyramid multi-view stereo net with self-adaptive view aggregation," in *ECCV*, 2020.
- [91] J. Yu, Z. Lin, J. Yang, X. Shen, X. Lu, and T. S. Huang, "Free-form image inpainting with gated convolution," in *ICCV*, 2019.
- [92] J. Zhang, Y. Yao, S. Li, Z. Luo, and T. Fang, "Visibility-aware multi-view stereo network," *BMVC*, 2020.
- [93] S. Xingjian, Z. Chen, H. Wang, D.-Y. Yeung, W.-K. Wong, and W.-c. Woo, "Convolutional lstm network: A machine learning approach for precipitation nowcasting," in *NIPS*, 2015.
- [94] X. Long, L. Liu, W. Li, C. Theobalt, and W. Wang, "Multi-view depth estimation using epipolar spatio-temporal networks," in *CVPR*, 2021, pp. 8258–8267.
- [95] R. Chen, S. Han, J. Xu, and H. Su, "Point-based multi-view stereo network," in *ICCV*, 2019.
- [96] K. Luo, T. Guan, L. Ju, H. Huang, and Y. Luo, "P-MVSNet: Learning patch-wise matching confidence aggregation for multi-view stereo," in *ICCV*, 2019.
- [97] S. Im, H.-G. Jeon, S. Lin, and I. S. Kweon, "Dpsnet: End-to-end deep plane sweep stereo," in *ICLR*, 2018.
- [98] K. Cho, B. V. Merriënboer, C. Gulcehre, D. Bahdanau, F. Bougares, H. Schwenk, and Y. Bengio, "Learning phrase representations using RNN encoder-decoder for statistical machine translation," *arXiv preprint arXiv:1406.1078*, 2014.
- [99] X. Wang, Z. Zhu, G. Huang, F. Qin, Y. Ye, Y. He, X. Chi, and X. Wang, "Mvster: epipolar transformer for efficient multi-view stereo," in *ECCV*. Springer, 2022, pp. 573–591.
- [100] X. Ma, Y. Gong, Q. Wang, J. Huang, L. Chen, and F. Yu, "Epp-mvsnet: Epipolar-assembling based depth prediction for multi-view stereo," in *ICCV*, 2021.
- [101] Z. Ma, Z. Teed, and J. Deng, "Multiview stereo with cascaded epipolar raft," *arXiv preprint arXiv:2205.04502*, 2022.
- [102] S. Wang, B. Li, and Y. Dai, "Efficient multi-view stereo by iterative dynamic cost volume," in *CVPR*, 2022, pp. 8655–8664.
- [103] J. Y. Lee, J. DeGol, C. Zou, and D. Hoiem, "Patchmatch-rl: Deep mvs with pixelwise depth, normal, and visibility," in *ICCV*, 2021, pp. 6158–6167.
- [104] C. Barnes, E. Shechtman, A. Finkelstein, and D. B. Goldman, "Patchmatch: A randomized correspondence algorithm for structural image editing," *ACM Trans. Graph.*, vol. 28, no. 3, 2009.
- [105] M. Bleyer, C. Rhemann, and C. Rother, "Patchmatch stereo - stereo matching with slanted support windows," in *BMVC*, 2011.
- [106] Z. Teed and J. Deng, "Raft: Recurrent all-pairs field transforms for optical flow," in *ECCV*, 2020.

- [107] L. Lipson, Z. Teed, and J. Deng, "Raft-stereo: Multilevel recurrent field transforms for stereo matching," in *2021 International Conference on 3D Vision (3DV)*. IEEE, 2021, pp. 218–227.
- [108] Z. Teed and J. Deng, "Raft-3d: Scene flow using rigid-motion embeddings," in *CVPR*, 2021, pp. 8375–8384.
- [109] X. Gu, W. Yuan, S. Dai, C. Tang, S. Zhu, and P. Tan, "Dro: Deep recurrent optimizer for structure-from-motion," *arXiv preprint arXiv:2103.13201*, 2021.
- [110] C. Sormann, E. Santellani, M. Rossi, A. Kuhn, and F. Fraundorfer, "Dels-mvs: Deep epipolar line search for multi-view stereo," in *WACV*, 2023.
- [111] C. Cai, P. Ji, Q. Yan, and Y. Xu, "Riav-mvs: Recurrent-indexing an asymmetric volume for multi-view stereo," in *CVPR*, 2023.
- [112] G. Xu, X. Wang, X. Ding, and X. Yang, "Iterative geometry encoding volume for stereo matching," in *CVPR*, 2023, pp. 21 919–21 928.
- [113] P. Knobelreiter, C. Sormann, A. Shekhovtsov, F. Fraundorfer, and T. Pock, "Belief propagation reloaded: Learning bp-layers for labeling problems," in *CVPR*, 2020.
- [114] R. Peng, R. Wang, Z. Wang, Y. Lai, and R. Wang, "Rethinking depth estimation for multi-view stereo: A unified representation," in *CVPR*, 2022, pp. 8645–8654.
- [115] X. Ye, W. Zhao, T. Liu, Z. Huang, Z. Cao, and X. Li, "Constraining depth map geometry for multi-view stereo: A dual-depth approach with saddle-shaped depth cells," in *ICCV*, 2023.
- [116] R. Chen, S. Han, J. Xu, and H. Su, "Visibility-aware point-based multi-view stereo network," *IEEE transactions on pattern analysis and machine intelligence*, vol. 43, no. 10, 2020.
- [117] Z. Yu and S. Gao, "Fast-mvsnet: Sparse-to-dense multi-view stereo with learned propagation and gauss-newton refinement," in *CVPR*, 2020.
- [118] T.-W. Hui, C. C. Loy, and X. Tang, "Depth map super-resolution by deep multi-scale guidance," in *ECCV*. Springer, 2016, pp. 353–369.
- [119] J. Xi, Y. Shi, Y. Wang, Y. Guo, and K. Xu, "Raymvsnet: Learning ray-based 1d implicit fields for accurate multi-view stereo," in *CVPR*, 2022, pp. 8595–8605.
- [120] Y. Shi, J. Xi, D. Hu, Z. Cai, and K. Xu, "Raymvsnet++: learning ray-based 1d implicit fields for accurate multi-view stereo," *IEEE Transactions on Pattern Analysis and Machine Intelligence*, 2023.
- [121] W. Su and W. Tao, "Efficient edge-preserving multi-view stereo network for depth estimation," in *AAAI*, 2023.
- [122] M. Poggi and S. Mattoccia, "Learning from scratch a confidence measure," in *BMVC*, 2016.
- [123] Z. Fu, M. Ardabilian, and G. Stern, "Stereo matching confidence learning based on multi-modal convolution neural networks," in *International Workshop on Representations, Analysis and Recognition of Shape and Motion From Imaging Data*. Springer, 2017.
- [124] F. Tosi, M. Poggi, A. Benincasa, and S. Mattoccia, "Beyond local reasoning for stereo confidence estimation with deep learning," in *ECCV*, 2018, pp. 319–334.
- [125] S. Kim, S. Kim, D. Min, and K. Sohn, "Laf-net: Locally adaptive fusion networks for stereo confidence estimation," in *CVPR*, 2019.
- [126] Z. Li, W. Zuo, Z. Wang, and L. Zhang, "Confidence-based large-scale dense multi-view stereo," *TIP*, vol. 29, 2020.
- [127] A. Kuhn, C. Sormann, M. Rossi, O. Erdler, and F. Fraundorfer, "Deepc-mvs: Deep confidence prediction for multi-view stereo reconstruction," in *3DV*. IEEE, 2020.
- [128] T.-Y. Lin, P. Goyal, R. Girshick, K. He, and P. Dollár, "Focal loss for dense object detection," in *ICCV*, 2017.
- [129] Y. Dai, Z. Zhu, Z. Rao, and B. Li, "Mvs2: Deep unsupervised multi-view stereo with multi-view symmetry," in *3DV*, 2019.
- [130] B. Huang, H. Yi, C. Huang, Y. He, J. Liu, and X. Liu, "M3vsnet: Unsupervised multi-metric multi-view stereo network," in *2021 IEEE International Conference on Image Processing (ICIP)*, 2021.
- [131] T. Khot, S. Agrawal, S. Tulsiani, C. Mertz, S. Lucey, and M. Hebert, "Learning unsupervised multi-view stereopsis via robust photometric consistency," *arXiv preprint arXiv:1905.02706*, 2019.
- [132] J. Yang, J. M. Alvarez, and M. Liu, "Self-supervised learning of depth inference for multi-view stereo," in *CVPR*, 2021.
- [133] F. Darmon, B. Basclé, J.-C. Devaux, P. Monasse, and M. Aubry, "Deep multi-view stereo gone wild," in *2021 International Conference on 3D Vision (3DV)*. IEEE, 2021.
- [134] Z. Wang, A. C. Bovik, H. R. Sheikh, and E. P. Simoncelli, "Image quality assessment: from error visibility to structural similarity," *IEEE transactions on image processing*, vol. 13, no. 4, 2004.
- [135] J. Zhang, R. Tang, Z. Cao, J. Xiao, R. Huang, and L. Fang, "Elasticmvs: Learning elastic part representation for self-supervised multi-view stereopsis," *Advances in Neural Information Processing Systems*, 2022.
- [136] K. Xiong, R. Peng, Z. Zhang, T. Feng, J. Jiao, F. Gao, and R. Wang, "Cl-mvsnet: Unsupervised multi-view stereo with dual-level contrastive learning," in *ICCV*, 2023.
- [137] F. Yang, Q. Sun, H. Jin, and Z. Zhou, "Superpixel segmentation with fully convolutional networks," in *CVPR*, 2020.
- [138] D. Sun, X. Yang, M.-Y. Liu, and J. Kautz, "Pwc-net: Cnns for optical flow using pyramid, warping, and cost volume," in *CVPR*, 2018.
- [139] G. Hinton, O. Vinyals, and J. Dean, "Distilling the knowledge in a neural network," *arXiv preprint arXiv:1503.02531*, 2015.
- [140] T. Furlanello, Z. Lipton, M. Tschannen, L. Itti, and A. Anandkumar, "Born again neural networks," in *ICML*, 2018.
- [141] Q. Xie, M.-T. Luong, E. Hovy, and Q. V. Le, "Self-training with noisy student improves imagenet classification," in *CVPR*, 2020.
- [142] A. Bozic, P. Palafox, J. Thies, A. Dai, and M. Nießner, "Transformerfusion: Monocular rgb scene reconstruction using transformers," *Advances in Neural Information Processing Systems*, vol. 34, 2021.
- [143] N. Stier, A. Rich, P. Sen, and T. Höllerer, "Vortx: Volumetric 3d reconstruction with transformers for voxelwise view selection and fusion," in *3DV*, 2021.
- [144] C. Sun, M. Sun, and H.-T. Chen, "Direct voxel grid optimization: Super-fast convergence for radiance fields reconstruction," in *CVPR*, 2022.
- [145] A. Chen, Z. Xu, A. Geiger, J. Yu, and H. Su, "Tensorf: Tensorial radiance fields," in *ECCV*, 2022.
- [146] T. Müller, A. Evans, C. Schied, and A. Keller, "Instant neural graphics primitives with a multiresolution hash encoding," *ACM Transactions on Graphics (ToG)*, vol. 41, no. 4, 2022.
- [147] J. T. Barron, B. Mildenhall, D. Verbin, P. P. Srinivasan, and P. Hedman, "Mip-nerf 360: Unbounded anti-aliased neural radiance fields," in *CVPR*, 2022.
- [148] S. Fridovich-Keil, A. Yu, M. Tancik, Q. Chen, B. Recht, and A. Kanazawa, "Plenoxels: Radiance fields without neural networks," in *CVPR*, 2022.
- [149] Z. Chen, T. Funkhouser, P. Hedman, and A. Tagliasacchi, "Mobilerf: Exploiting the polygon rasterization pipeline for efficient neural field rendering on mobile architectures," in *CVPR*, 2023.
- [150] J. T. Barron, B. Mildenhall, D. Verbin, P. P. Srinivasan, and P. Hedman, "Zip-nerf: Anti-aliased grid-based neural radiance fields," in *ICCV*, 2023.
- [151] C. Reiser, R. Szeliski, D. Verbin, P. Srinivasan, B. Mildenhall, A. Geiger, J. Barron, and P. Hedman, "Merf: Memory-efficient radiance fields for real-time view synthesis in unbounded scenes," *ACM Transactions on Graphics (TOG)*, vol. 42, no. 4, 2023.
- [152] Q. Gao, Q. Xu, H. Su, U. Neumann, and Z. Xu, "Strivec: Sparse tri-vector radiance fields," in *ICCV*, 2023.
- [153] Y. Wei, S. Liu, Y. Rao, W. Zhao, J. Lu, and J. Zhou, "Nerfingmvs: Guided optimization of neural radiance fields for indoor multi-view stereo," in *ICCV*, 2021.
- [154] Z. Yu, S. Peng, M. Niemeyer, T. Sattler, and A. Geiger, "Monosdf: Exploring monocular geometric cues for neural implicit surface reconstruction," *Advances in neural information processing systems*, 2022.
- [155] J. Wang, P. Wang, X. Long, C. Theobalt, T. Komura, L. Liu, and W. Wang, "Neuris: Neural reconstruction of indoor scenes using normal priors," in *ECCV*, 2022.
- [156] Q. Fu, Q. Xu, Y. S. Ong, and W. Tao, "Geo-neus: Geometry-consistent neural implicit surfaces learning for multi-view reconstruction," *Advances in Neural Information Processing Systems*, 2022.
- [157] Y. Wang, Q. Han, M. Habermann, K. Daniilidis, C. Theobalt, and L. Liu, "Neus2: Fast learning of neural implicit surfaces for multi-view reconstruction," in *ICCV*, 2023.
- [158] Z. Li, T. Müller, A. Evans, R. H. Taylor, M. Unberath, M.-Y. Liu, and C.-H. Lin, "Neuralangelo: High-fidelity neural surface reconstruction," in *CVPR*, 2023.
- [159] R. A. Rosu and S. Behnke, "Permutosdf: Fast multi-view reconstruction with implicit surfaces using permutohedral lattices," in *CVPR*, 2023.
- [160] F. Wang, M.-J. Rakotosaona, M. Niemeyer, R. Szeliski, M. Pollefeys, and F. Tombari, "Unisdf: Unifying neural representations for high-fidelity 3d reconstruction of complex scenes with reflections," *arXiv preprint arXiv:2312.13285*, 2023.
- [161] X. Long, C. Lin, P. Wang, T. Komura, and W. Wang, "Sparseneus: Fast generalizable neural surface reconstruction from sparse views," in *ECCV*, 2022.
- [162] Y. Ren, F. Wang, T. Zhang, M. Pollefeys, and S. Süsstrunk, "Volrecon: Volume rendering of signed ray distance functions for generalizable multi-view reconstruction," in *CVPR*, 2023.

- [163] Y. Liang, H. He, and Y.-C. Chen, "Retr: Modeling rendering via transformer for generalizable neural surface reconstruction," in *Advances in neural information processing systems*, 2023.
- [164] D. Verbin, P. Hedman, B. Mildenhall, T. Zickler, J. T. Barron, and P. P. Srinivasan, "Ref-nerf: Structured view-dependent appearance for neural radiance fields," in *CVPR*, 2022.
- [165] L. Yariv, P. Hedman, C. Reiser, D. Verbin, P. P. Srinivasan, R. Szeliski, J. T. Barron, and B. Mildenhall, "Baked sdf: Meshing neural sdf for real-time view synthesis," in *ACM SIGGRAPH 2023 Conference Proceedings*, 2023.
- [166] Y. Liu, P. Wang, C. Lin, X. Long, J. Wang, L. Liu, T. Komura, and W. Wang, "Nero: Neural geometry and brdf reconstruction of reflective objects from multiview images," *arXiv preprint arXiv:2305.17398*, 2023.
- [167] R. Liang, H. Chen, C. Li, F. Chen, S. Panneer, and N. Vijaykumar, "Env-vidr: Implicit differentiable renderer with neural environment lighting," in *ICCV*, 2023.
- [168] W. Ge, T. Hu, H. Zhao, S. Liu, and Y.-C. Chen, "Ref-neus: Ambiguity-reduced neural implicit surface learning for multi-view reconstruction with reflection," in *ICCV*, 2023.
- [169] B. Mildenhall, P. P. Srinivasan, M. Tancik, J. T. Barron, R. Ramamoorthi, and R. Ng, "Nerf: Representing scenes as neural radiance fields for view synthesis," *Communications of the ACM*, vol. 65, no. 1, 2021.
- [170] B. Kerbl, G. Kopanas, T. Leimkühler, and G. Drettakis, "3d gaussian splatting for real-time radiance field rendering," *ACM Transactions on Graphics*, vol. 42, no. 4, 2023.
- [171] N. Snavely, S. M. Seitz, and R. Szeliski, "Photo tourism: exploring photo collections in 3d," in *ACM siggraph 2006 papers*, 2006, pp. 835–846.
- [172] M. Kazhdan, M. Bolitho, and H. Hoppe, "Poisson surface reconstruction," in *Proceedings of the fourth Eurographics symposium on Geometry processing*, vol. 7, no. 4, 2006.
- [173] H. Chen, C. Li, and G. H. Lee, "Neusg: Neural implicit surface reconstruction with 3d gaussian splatting guidance," *arXiv preprint arXiv:2312.00846*, 2023.
- [174] A. Vaswani, N. Shazeer, N. Parmar, J. Uszkoreit, L. Jones, A. N. Gomez, L. Kaiser, and I. Polosukhin, "Attention is all you need," *Advances in neural information processing systems*, 2017.
- [175] J. Han, F. Kokkinos, and P. Torr, "Vfusion3d: Learning scalable 3d generative models from video diffusion models," *arXiv preprint arXiv:2403.12034*, 2024.
- [176] D. Tochilkin, D. Pankratz, Z. Liu, Z. Huang, A. Letts, Y. Li, D. Liang, C. Laforte, V. Jampani, and Y.-P. Cao, "Triposr: Fast 3d object reconstruction from a single image," *arXiv preprint arXiv:2403.02151*, 2024.
- [177] J. Li, H. Tan, K. Zhang, Z. Xu, F. Luan, Y. Xu, Y. Hong, K. Sunkavalli, G. Shakhnarovich, and S. Bi, "Instant3d: Fast text-to-3d with sparse-view generation and large reconstruction model," *ICLR*, 2024.
- [178] Y. Xu, H. Tan, F. Luan, S. Bi, P. Wang, J. Li, Z. Shi, K. Sunkavalli, G. Wetzstein, Z. Xu *et al.*, "Dmv3d: Denoising multi-view diffusion using 3d large reconstruction model," *ICLR*, 2024.
- [179] P. Wang, H. Tan, S. Bi, Y. Xu, F. Luan, K. Sunkavalli, W. Wang, Z. Xu, and K. Zhang, "Pf-lrm: Pose-free large reconstruction model for joint pose and shape prediction," *ICLR*, 2024.
- [180] E. R. Chan, C. Z. Lin, M. A. Chan, K. Nagano, B. Pan, S. De Mello, O. Gallo, L. J. Guibas, J. Tremblay, S. Khamis *et al.*, "Efficient geometry-aware 3d generative adversarial networks," in *CVPR*, 2022.
- [181] A. Dosovitskiy, L. Beyer, A. Kolesnikov, D. Weissenborn, X. Zhai, T. Unterthiner, M. Dehghani, M. Minderer, G. Heigold, S. Gelly *et al.*, "An image is worth 16x16 words: Transformers for image recognition at scale," *arXiv preprint arXiv:2010.11929*, 2020.
- [182] K. Luo, T. Guan, L. Ju, H. Huang, and Y. Luo, "P-mvsnet: Learning patch-wise matching confidence aggregation for multi-view stereo," in *ICCV*, 2019, pp. 10452–10461.
- [183] Z. Wei, Q. Zhu, C. Min, Y. Chen, and G. Wang, "Bidirectional hybrid lstm based recurrent neural network for multi-view stereo," *IEEE Transactions on Visualization and Computer Graphics*, 2022.
- [184] K. Luo, T. Guan, L. Ju, Y. Wang, Z. Chen, and Y. Luo, "Attention-aware multi-view stereo," in *CVPR*, 2020.
- [185] J. Yang, J. M. Alvarez, and M. Liu, "Non-parametric depth distribution modelling based depth inference for multi-view stereo," in *CVPR*, 2022, pp. 8626–8634.
- [186] L. Wang, Y. Gong, X. Ma, Q. Wang, K. Zhou, and L. Chen, "Is-mvsnet: Importance sampling-based mvsnet," in *ECCV*. Springer, 2022, pp. 668–683.
- [187] Q. Zhu, Z. Wei, Z. Wang, Y. Chen, and G. Wang, "Hybrid cost volume regularization for memory-efficient multi-view stereo networks," in *BMVC*, 2022.
- [188] Y. Zhang, J. Zhu, and L. Lin, "Multi-view stereo representation revisited: Region-aware mvsnet," in *CVPR*, 2023, pp. 17376–17385.
- [189] Q. Xu, W. Kong, W. Tao, and M. Pollefeys, "Multi-scale geometric consistency guided and planar prior assisted multi-view stereo," *IEEE Transactions on Pattern Analysis and Machine Intelligence*, 2022.
- [190] Y. Wang, I. Skorokhodov, and P. Wonka, "Hf-neus: Improved surface reconstruction using high-frequency details," *Advances in Neural Information Processing Systems*, 2022.
- [191] J. Zhang, Y. Yao, S. Li, T. Fang, D. McKinnon, Y. Tsing, and L. Quan, "Critical regularizations for neural surface reconstruction in the wild," in *CVPR*, 2022.
- [192] Y. Wang, I. Skorokhodov, and P. Wonka, "Pet-neus: Positional encoding tri-planes for neural surfaces," in *CVPR*, 2023.
- [193] T. Wu, J. Wang, X. Pan, X. Xu, C. Theobalt, Z. Liu, and D. Lin, "Voxurf: Voxel-based efficient and accurate neural surface reconstruction," *arXiv preprint arXiv:2208.12697*, 2022.
- [194] K. Zhang, S. Bi, H. Tan, Y. Xiangli, N. Zhao, K. Sunkavalli, and Z. Xu, "Gs-lrm: Large reconstruction model for 3d gaussian splatting," *arXiv preprint arXiv:2404.19702*, 2024.
- [195] J. Tang, Z. Chen, X. Chen, T. Wang, G. Zeng, and Z. Liu, "Lgm: Large multi-view gaussian model for high-resolution 3d content creation," *arXiv preprint arXiv:2402.05054*, 2024.
- [196] W. Wang, D. Zhu, X. Wang, Y. Hu, Y. Qiu, C. Wang, Y. Hu, A. Kapoor, and S. Scherer, "Tartanair: A dataset to push the limits of visual slam," in *IROS*, 2020.
- [197] G. Baruch, Z. Chen, A. Dehghan, T. Dimry, Y. Feigin, P. Fu, T. Gebauer, B. Joffe, D. Kurz, A. Schwartz *et al.*, "Arkitscenes: A diverse real-world dataset for 3d indoor scene understanding using mobile rgb-d data," *arXiv preprint arXiv:2111.08897*, 2021.
- [198] C. Yeshwanth, Y.-C. Liu, M. Nießner, and A. Dai, "Scannet++: A high-fidelity dataset of 3d indoor scenes," in *ICCV*, 2023.
- [199] J. Deng, W. Dong, R. Socher, L.-J. Li, K. Li, and L. Fei-Fei, "Imagenet: A large-scale hierarchical image database," in *CVPR*, 2009.
- [200] X. Yu, M. Xu, Y. Zhang, H. Liu, C. Ye, Y. Wu, Z. Yan, C. Zhu, Z. Xiong, T. Liang *et al.*, "Mvimgnet: A large-scale dataset of multi-view images," in *CVPR*, 2023.
- [201] P.-E. Sarlin, M. Dusmanu, J. L. Schönberger, P. Speciale, L. Gruber, V. Larsson, O. Miksik, and M. Pollefeys, "Lamar: Benchmarking localization and mapping for augmented reality," in *ECCV*, 2022.
- [202] S. Weder, J. Schonberger, M. Pollefeys, and M. R. Oswald, "Routefusion: Learning real-time depth map fusion," in *CVPR*, 2020, pp. 4887–4897.
- [203] S. Weder, J. L. Schonberger, M. Pollefeys, and M. R. Oswald, "Neuralfusion: Online depth fusion in latent space," in *CVPR*, 2021, pp. 3162–3172.
- [204] J. Dai, H. Qi, Y. Xiong, Y. Li, G. Zhang, H. Hu, and Y. Wei, "Deformable convolutional networks," in *ICCV*, 2017.
- [205] K. Wu, J. Zhang, H. Peng, M. Liu, B. Xiao, J. Fu, and L. Yuan, "Tinyvit: Fast pretraining distillation for small vision transformers," in *ECCV*, 2022.
- [206] U. Kusunoki, S. Cheng, R. Chen, and H. Su, "Normal assisted stereo depth estimation," in *CVPR*, 2020.
- [207] X. Long, L. Liu, C. Theobalt, and W. Wang, "Occlusion-aware depth estimation with adaptive normal constraints," in *ECCV*, 2020.
- [208] C. Liu, K. Kim, J. Gu, Y. Furukawa, and J. Kautz, "PlanerCNN: 3d plane detection and reconstruction from a single image," in *CVPR*, 2019.
- [209] H. Liu, X. Tang, and S. Shen, "Depth-map completion for large indoor scene reconstruction," *Pattern Recognition*, vol. 99, p. 107112, 2020.
- [210] A. Eftekhar, A. Sax, J. Malik, and A. Zamir, "Omnidata: A scalable pipeline for making multi-task mid-level vision datasets from 3D scans," in *ICCV*, 2021.
- [211] J. Liu, P. Ji, N. Bansal, C. Cai, Q. Yan, X. Huang, and Y. Xu, "Planemvs: 3d plane reconstruction from multi-view stereo," in *CVPR*, 2022.
- [212] Y. Xie, M. Gadelha, F. Yang, X. Zhou, and H. Jiang, "PlanarRecon: Real-time 3d plane detection and reconstruction from posed monocular videos," in *CVPR*, 2022.
- [213] A. Osman Ulusoy, M. J. Black, and A. Geiger, "Semantic multi-view stereo: Jointly estimating objects and voxels," in *CVPR*, 2017.
- [214] E.-K. Stathopoulou and F. Remondino, "Semantic photogrammetry-boosting image-based 3d reconstruction with semantic labeling," *The International Archives of the Photogrammetry, Remote Sensing and Spatial Information Sciences*, vol. 42, pp. 685–690, 2019.

- [215] E. K. Stathopoulou, R. Battisti, D. Cernea, F. Remondino, and A. Georgopoulos, "Semantically derived geometric constraints for mvs reconstruction of textureless areas," *Remote Sensing*, vol. 13, no. 6, p. 1053, 2021.
- [216] H. Guo, S. Peng, H. Lin, Q. Wang, G. Zhang, H. Bao, and X. Zhou, "Neural 3d scene reconstruction with the manhattan-world assumption," in *CVPR*, 2022.